HAL
archives-ouvertes.fr

A LINEARITY PRESERVING CELL-CENTERED SCHEME FOR THE HETEROGENEOUS AND ANISOTROPIC DIFFUSION EQUATIONS ON GENERAL MESHES

Gao Zhiming, Wu Jiming

▶ To cite this version:

Gao Zhiming, Wu Jiming. A LINEARITY PRESERVING CELL-CENTERED SCHEME FOR THE HETEROGENEOUS AND ANISOTROPIC DIFFUSION EQUATIONS ON GENERAL MESHES. [Research Report] 2011. <inria-00481112v2>

HAL Id: inria-00481112
https://hal.inria.fr/inria-00481112v2

Submitted on 16 Nov 2013

HAL is a multi-disciplinary open access archive for the deposit and dissemination of scientific research documents, whether they are published or not. The documents may come from teaching and research institutions in France or abroad, or from public or private research centers.

L'archive ouverte pluridisciplinaire **HAL**, est destinée au dépôt et à la diffusion de documents scientifiques de niveau recherche, publiés ou non, émanant des établissements d'enseignement et de recherche français ou étrangers, des laboratoires publics ou privés.

INTERNATIONAL JOURNAL FOR NUMERICAL METHODS IN FLUIDS
Int. J. Numer. Meth. Fluids 2011; **67**:2157–2183
Published online 10 December 2010 in Wiley Online Library (wileyonlinelibrary.com). DOI: 10.1002/fld.2496

A linearity-preserving cell-centered scheme for the heterogeneous and anisotropic diffusion equations on general meshes

Zhiming Gao and Jiming Wu*, †

Laboratory of Computational Physics, Institute of Applied Physics and Computational Mathematics, P.O. Box 8009-26, Beijing 100088, People's Republic of China

SUMMARY

In this paper a finite volume scheme for the heterogeneous and anisotropic diffusion equations is proposed on general, possibly nonconforming meshes. This scheme has both cell-centered unknowns and vertex unknowns. The vertex unknowns are treated as intermediate ones and are expressed as a linear weighted combination of the surrounding cell-centered unknowns, which reduces the scheme to a completely cell-centered one. We propose two types of new explicit weights which allow arbitrary diffusion tensors, and are neither discontinuity dependent nor mesh topology dependent. Both the derivation of the scheme and that of new weights satisfy the linearity-preserving criterion which requires that a discretization scheme should be exact on linear solutions. The resulting new scheme is called as the linearity-preserving cell-centered scheme and the numerical results show that it maintain optimal convergence rates for the solution and flux on general polygonal distorted meshes in case that the diffusion tensor is taken to be anisotropic, at times heterogeneous, and/or discontinuous. Copyright © 2010 John Wiley & Sons, Ltd.

Received 17 June 2010; Revised 23 August 2010; Accepted 24 October 2010

KEY WORDS: diffusion equation; anisotropic diffusion tensor; cell-centered scheme; linearity-preserving criterion; nonconforming mesh

1. INTRODUCTION

This paper will focus on the investigation of new discretization scheme for solving the anisotropic steady-state diffusion equation

$$-\mathrm{div}(K\nabla u) = f \quad \text{in } \Omega, \tag{1a}$$

$$u = g_{\mathrm{D}} \quad \text{on } \Gamma_{\mathrm{D}}, \tag{1b}$$

$$-K\nabla u \cdot \mathbf{n} = g_{\mathrm{N}} \quad \text{on } \Gamma_{\mathrm{N}}, \tag{1c}$$

where $K(x, y)$ is a 2×2 diffusion tensor, f is the source term, Ω is a bounded polygonal domain in R^2 with its boundary $\partial\Omega = \bar{\Gamma}_{\mathrm{D}} \cup \bar{\Gamma}_{\mathrm{N}}$, where the Dirichlet and Neumann boundary conditions are imposed on Γ_{D} and Γ_{N}, respectively. $\mathbf{n}$ denotes the outward unit vector normal to the boundary $\partial\Omega$ and g_{D}, g_{N} are given scalar functions which are almost everywhere defined on Γ_{D}, Γ_{N}, respectively.

Equations of this kind arise in a wide range of scientific fields such as hydrogeology, oil reservoir simulations, plasma physics, semiconductor modeling, Navier–Stokes equations, biology, and so on.

*Correspondence to: Jiming Wu, Laboratory of Computational Physics, Institute of Applied Physics and Computational Mathematics, P.O. Box 8009-26, Beijing 100088, People's Republic of China.
†E-mail: wu_jiming@iapcm.ac.cn

Copyright © 2010 John Wiley & Sons, Ltd.

For example, in porous media u is called pressure, the diffusion tensor K may be highly anisotropic, heterogeneous and/or discontinuous, which imposes a great challenge for discretization schemes. In addition, another difficulty is that the computational mesh is usually nonconforming, highly distorted and highly skewed in some applications such as laser-driven inertial confinement fusion.

The development of a discretization scheme should be based on the requirements motivated by both practical implementation and physical background, the issues about which range from the classical stability and accuracy to some other desirable numerical properties, local stencil, local conservation, monotonicity, allowing arbitrary diffusion tensors, simplicity, robustness, cost-efficiency and so on. To our knowledge, there exists no scheme satisfying all the above properties. Among the aforementioned desirable properties, from our point of view, accuracy, cost-efficiency and allowing arbitrary diffusion tensors are among the fundamental ones.

We are interested in the discretization scheme which satisfies the so-called *linearity-preserving criterion*, which requires that each step of the derivation of a discretization scheme for diffusion equation is exact or linearly exact, i.e. exact in the sense whenever the solution is a linear function and the diffusion coefficient is a constant tensor. We observe that some authors mentioned linearity-preserving criterion in their works [1–5]. To our knowledge, the authors usually claimed that certain scheme satisfies or does not satisfy the linearity-preserving criterion without intensive investigation. Although the linearity-preserving criterion, at the present, has not been theoretically proved to be a sufficient or necessary condition for certain good numerical properties mentioned above, we observe from our numerical practice and other peoples' works that a discretization scheme under linearity-preserving criterion usually maintains good accuracy on highly distorted meshes. Our point of view is confirmed once again by a recent work [4]. This scheme keeps all good numerical properties that a desirable mimetic finite difference scheme can have, except the linearity-preserving property. Numerical experiments done by the authors show that this scheme performs poorly on many distorted quadrilateral meshes. Motivated by the above observation, we will suggest a new discretization scheme under linearity-preserving criterion in this paper.

In this paper, under the linearity-preserving criterion, we propose a new finite volume scheme for the anisotropic diffusion equations on general meshes. In this scheme, the flux on each cell edge is explicitly expressed by two cell-centered unknowns defined on the cells sharing that edge, and two vertex unknowns at the two endpoints. A certain treatment for the vertex unknowns must be taken into account and the simplest and common way is to treat them as intermediate ones, more specifically, express them as certain linear combinations of the neighboring cell-centered unknowns. The coefficients in the linear combinations are known as the weights. To our knowledge, there exists in the literature some ways to find the weights for the vertex unknowns, such as by Taylor expansion [6, 7], by a straightforward bilinear interpolation [8] or its modification [9], by finite point method [10] or by some others [11]. Most of these methods are obtained in the isotropic case, and all these methods are either *discontinuity dependent* or *mesh topology dependent*. That a method is discontinuity dependent means that the derivation and display of the weights must be done under the condition that the location of the discontinuity is known beforehand. The implementation of a discontinuity-dependent method will encounter difficulties and troubles when some moving discontinuity, such as shock wave, is presented. If a method for derivation of the weights is done under the condition that an interior vertex should meet four cell edges and its extension to the boundary vertex is not straightforward, it is called here mesh topology dependent. Obviously, it is difficult or complicated to extend a topology-dependent method to the unstructured or nonconforming meshes. A linear least-square approximation to calculate the weights is proposed in [12] and a generalization of this strategy for a more accurate reconstruction of the Neumann boundary vertex unknowns is developed in [13]. The weights in [13] is neither discontinuity dependent nor mesh topology dependent, but is not physically reasonable since the diffusion tensor is not taken into account.

Recently, a new approach in [14] has a desirable accuracy on highly distorted quadrilateral meshes, but it is a little complicate and involves a large amount of extra computational cost. A further improvement, with much reduced extra computational cost, was proposed in [15] by

Copyright © 2010 John Wiley & Sons, Ltd.

DOI: 10.1002/fld

employing a multi-point flux approximation (MPFA) technique. These two types of weights are not discontinuity dependent and the latter is even not mesh topology dependent, however, they are not given explicitly, instead, they are evaluated by solving certain local linear systems whose solvability itself is often proved to be a difficult problem. In addition, in the construction of other discretization schemes such as the local support operator scheme [3], the local flux mimetic finite difference scheme [16], the physical space-derived MPFA [17, 18] together with its variations [19], and the reference space-derived MPFA [20, 21], the solution of certain local linear system is also required.

The above observations have motivated us to propose two types of new weights for the proposed scheme, and the solution of certain local linear systems is avoided. Our new scheme has the following characteristics:

- it has only cell-centered unknowns and a local stencil;
- it satisfies the linearity-preserving criterion;
- it allows arbitrary diffusion tensors;
- it leads to a nine-point scheme in case of structured quadrilateral meshes;
- it is neither discontinuity dependent nor mesh topology dependent;
- it has second-order convergence rate for the approximate solution and higher than first-order accuracy for the flux on general meshes;
- the explicit weights in this scheme are easy to code and have low computational costs.

The remainder of this paper is organized as follows. In Section 2, we derive the linearity-preserving cell-centered scheme. The numerical results are presented in Section 3 to show the accuracy and efficiency of the linearity preserving cell-centered scheme and some conclusions are given in the last section.

2. CONSTRUCTION OF THE SCHEME

This section is devoted to the derivation of the new scheme under the linearity-preserving criterion. To begin with, we introduce the flux vector $\mathbf{F}$

$$\mathbf{F} = -K\nabla u. \tag{2}$$

Then the model equation (1a) can be rewritten as:

$$\operatorname{div}\mathbf{F} = f \quad \text{in } \Omega. \tag{3}$$

Following the idea of the finite volume framework, the above equation is integrated over each control volume e, usually a polygonal cell, which formally gives the following balance equation by using the Gauss divergence theorem

$$\int_{\partial e} \mathbf{F}\cdot\mathbf{n_e}\mathrm{d}s = \iint_e f(x,y)\mathrm{d}x\mathrm{d}y, \tag{4}$$

where $\mathbf{n}_e$ denotes the outward unit vector normal to the cell boundary ∂e. The control volume method is now down to find a discrete expression for the integration of $\mathbf{F}\cdot\mathbf{n_e}$ along each cell edge.

Specifically, in this paper, we shall derive a discrete expression for the integration of $\mathbf{F}\cdot\mathbf{n_e}$ on each cell edge which is explicitly expressed by the two cell-centered unknowns defined on the cells sharing that edge, and the two vertex unknowns at the two endpoints of the edge. The derivation of the scheme will be subjected to the linearity-preserving criterion, which requires that each step of the derivation of a discretization scheme for (1a) is exact or linearly exact in the sense whenever the equation possesses a piecewise linear solution and the diffusion coefficient is a constant tensor. Throughout, we shall endow the symbol $\simeq$ with a special meaning and assume that

- $=$ is used if the derivation is exact;
- $\simeq$ is used whenever the relevant approximation satisfies the linearity preserving criterion;

Copyright © 2010 John Wiley & Sons, Ltd.

DOI: 10.1002/fld

- $\approx$, by contrast, will be used when an approximation is not subjected to the linearity-preserving criterion.

2.1. Discretization of the flux

This subsection is devoted to derive the expression for the flux on each cell edge under the linearity-preserving criterion. We begin the derivation by introducing the following lemma.

Lemma 2.1
Let $\triangle OPQ$ be a triangle with vertices O, P, Q ordered counterclockwise. For a function u defined on $\triangle OPQ$, we have

$$\nabla u \simeq \frac{1}{2S_{\triangle OPQ}}[(u_P - u_O)\mathscr{R}\overrightarrow{OQ} + (u_Q - u_O)\mathscr{R}\overrightarrow{PO}] \tag{5}$$

and

$$\nabla u \simeq \frac{u_Q - u_P}{|PQ|^2}\overrightarrow{PQ} + \frac{\mathscr{R}\overrightarrow{PQ}}{|PQ|^2}[(u_P - u_O)\cot\angle PQO + (u_Q - u_O)\cot\angle OPQ], \tag{6}$$

where $S_{\triangle OPQ}$ is the area of $\triangle OPQ$, u_O,u_P,u_Q are the values of u at vertices O,P,Q, respectively, and the matrix $\mathscr{R}$ is defined by:

$$\mathscr{R} = \mathscr{R}_{\frac{\pi}{2}}, \quad \mathscr{R}_\theta = \begin{pmatrix} \cos\theta & \sin\theta \\ -\sin\theta & \cos\theta \end{pmatrix}.$$

Proof
Formula (5) can be found in many papers, such as [13, 17]. For the self-completeness of the present paper, we give its proof. Under the linearity-preserving criterion, the gradient ∇u is a constant vector on $\triangle OPQ$ so that,

$$\begin{pmatrix} u_P - u_O \\ u_Q - u_O \end{pmatrix} \simeq \begin{pmatrix} \overrightarrow{OP}^{\mathrm{T}} \\ \overrightarrow{OQ}^{\mathrm{T}} \end{pmatrix} \nabla u := X\nabla u.$$

Since the inverse of X can be expressed as

$$X^{-1} = \frac{1}{\det X}(\mathscr{R}\overrightarrow{OQ} \quad \mathscr{R}\overrightarrow{PO}) = \frac{1}{2S_{\triangle OPQ}}(\mathscr{R}\overrightarrow{OQ} \quad \mathscr{R}\overrightarrow{PO}),$$

we obtain (5) and by noting

$$\frac{\mathscr{R}\overrightarrow{PO}}{2S_{\triangle OPQ}} = \frac{1}{|PQ|^2}\overrightarrow{PQ} + \frac{\cot\angle OPQ}{|PQ|^2}\mathscr{R}\overrightarrow{PQ},$$

$$\frac{\mathscr{R}\overrightarrow{OQ}}{2S_{\triangle OPQ}} = -\frac{1}{|PQ|^2}\overrightarrow{PQ} + \frac{\cot\angle PQO}{|PQ|^2}\mathscr{R}\overrightarrow{PQ},$$

we reach (6) which ends the proof. □

Now, we suppose that the computational domain Ω is partitioned into a number of non-overlapping regular polygonal cells. As shown in Figure 1, we shall use the following notations to derive our scheme:

- O_A is the cell center of an arbitrary cell $A_1A_2\ldots A_k$, and O_B is the cell center of its neighboring cell $B_1B_2\ldots B_m$;
- $\boldsymbol{n}_A$ is the outward unit vector normal to the cell boundary $\partial A_1A_2\ldots A_k$, and $\boldsymbol{n}_B$ is the outward unit vector normal to the cell boundary $\partial B_1B_2\ldots B_m$;

Copyright © 2010 John Wiley & Sons, Ltd.

DOI: 10.1002/fld

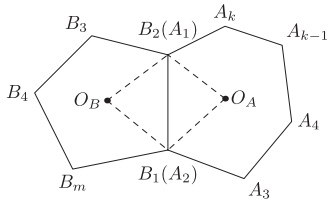

Figure 1. A local diagram of the polygonal mesh.

- $h_A^{(i)}$ is the distance from O_A to A_iA_{i+1} with $A_{k+1}=A_1$, and $h_B^{(i)}$ is the distance from O_B to B_iB_{i+1} with $B_{m+1}=B_1$;
- $K_\alpha=K(x_{O_\alpha}, y_{O_\alpha})$, $\alpha=A, B$;
- u_A, u_B are the approximations of u on two cells $A_1A_2\ldots A_k$ and $B_1B_2\ldots B_m$, respectively, and u_{A_i}, u_{B_i} denote the approximations of u at the vertices A_i, B_i.

With these notations, we are ready to describe our method. To begin with, we derive the discrete flux across an internal edge. Using Lemma 2.1 on the triangle $O_BB_1B_2$, we obtain

$$\nabla u \simeq \frac{\mathscr{R}\overrightarrow{B_1B_2}}{|B_1B_2|^2}[(u_{B_1}-u_B)\cot\angle B_1B_2O_B+(u_{B_2}-u_B)\cot\angle O_BB_1B_2]+(u_{B_2}-u_{B_1})\frac{\overrightarrow{B_1B_2}}{|B_1B_2|^2}.$$

Since we have the following identity:

$$K_B^{\mathrm{T}}\mathscr{R}\overrightarrow{B_1B_2}=K_B^{(t)}\overrightarrow{B_1B_2}+K_B^{(n)}(\mathscr{R}\overrightarrow{B_1B_2}),$$

where

$$K_\alpha^{(n)}=\frac{(\mathscr{R}\overrightarrow{B_1B_2})^{\mathrm{T}}K_\alpha(\mathscr{R}\overrightarrow{B_1B_2})}{|B_1B_2|^2},\quad K_\alpha^{(t)}=\frac{(\mathscr{R}\overrightarrow{B_1B_2})^{\mathrm{T}}K_\alpha\overrightarrow{B_1B_2}}{|B_1B_2|^2},\quad \alpha=A,B,$$

then we have

$$\boldsymbol{F}\cdot(\mathscr{R}\overrightarrow{B_1B_2})\simeq -K_B^{(n)}[(u_{B_1}-u_B)\cot\angle B_1B_2O_B+(u_{B_2}-u_B)\cot\angle O_BB_1B_2]-(u_{B_2}-u_{B_1})K_B^{(t)},$$

or equivalently

$$\boldsymbol{F}\cdot(\mathscr{R}\overrightarrow{B_1B_2})\simeq -\frac{K_B^{(n)}}{h_B^{(1)}|B_1B_2|}[(\overrightarrow{B_2O_B}\cdot\overrightarrow{B_2B_1})(u_{B_1}-u_B)+(\overrightarrow{B_1O_B}\cdot\overrightarrow{B_1B_2})(u_{B_2}-u_B)]$$
$$-(u_{B_2}-u_{B_1})K_B^{(t)}.$$

It follows that

$$\frac{h_B^{(1)}}{K_B^{(n)}}\int_{B_1B_2}\boldsymbol{F}\cdot\boldsymbol{n}_B\,\mathrm{d}s\simeq -\frac{1}{|B_1B_2|}[(\overrightarrow{B_2O_B}\cdot\overrightarrow{B_2B_1})(u_{B_1}-u_B)+(\overrightarrow{B_1O_B}\cdot\overrightarrow{B_1B_2})(u_{B_2}-u_B)]$$
$$-(u_{B_2}-u_{B_1})\frac{h_B^{(1)}K_B^{(t)}}{K_B^{(n)}}. \tag{7}$$

Analogously on the triangular domain $O_AA_1A_2$,

$$\frac{h_A^{(1)}}{K_A^{(n)}}\int_{B_1B_2}\boldsymbol{F}\cdot\boldsymbol{n}_A\,\mathrm{d}s\simeq -\frac{1}{|A_1A_2|}[(\overrightarrow{B_1O_A}\cdot\overrightarrow{B_1B_2})(u_{B_2}-u_A)+(\overrightarrow{B_2O_A}\cdot\overrightarrow{B_2B_1})(u_{B_1}-u_A)]$$
$$-(u_{B_1}-u_{B_2})\frac{h_A^{(1)}K_A^{(t)}}{K_A^{(n)}}. \tag{8}$$

Copyright © 2010 John Wiley & Sons, Ltd.

DOI: 10.1002/fld

Since the flux is continuous across the cell edge B_1B_2,

$$\int_{B_1B_2} \boldsymbol{F}\cdot\boldsymbol{n}_A \,\mathrm{d}s + \int_{B_1B_2} \boldsymbol{F}\cdot\boldsymbol{n}_B \,\mathrm{d}s = 0,$$

from (8), we obtain

$$\frac{h_A^{(1)}}{K_A^{(n)}} \int_{B_1B_2} \boldsymbol{F}\cdot\boldsymbol{n}_B \,\mathrm{d}s \simeq \frac{1}{|A_1A_2|}[(\overrightarrow{B_1O_A}\cdot\overrightarrow{B_1B_2})(u_{B_2}-u_A)+(\overrightarrow{B_2O_A}\cdot\overrightarrow{B_2B_1})(u_{B_1}-u_A)]$$

$$+(u_{B_1}-u_{B_2})\frac{h_A^{(1)}K_A^{(t)}}{K_A^{(n)}}. \tag{9}$$

Finally, by taking an average from (7) and (9), we have the following discretization of the flux on the interior edge B_1B_2:

$$\int_{B_1B_2} \boldsymbol{F}\cdot\boldsymbol{n}_B \,\mathrm{d}s \simeq -\mathscr{K}_{AB}^{(1)}|B_1B_2|[u_A-u_B-\mathscr{D}_{AB}^{(1)}(u_{B_2}-u_{B_1})], \tag{10}$$

where

$$\mathscr{K}_{AB}^{(1)} = \frac{K_A^{(n)}K_B^{(n)}}{K_A^{(n)}h_B^{(1)}+K_B^{(n)}h_A^{(1)}}, \quad \mathscr{D}_{AB}^{(1)} = \frac{\overrightarrow{B_1B_2}\cdot\overrightarrow{O_BO_A}}{|B_1B_2|^2} - \frac{1}{|B_1B_2|}\left(\frac{K_B^{(t)}}{K_B^{(n)}}h_B^{(1)}+\frac{K_A^{(t)}}{K_A^{(n)}}h_A^{(1)}\right).$$

The expressions of the normal component of the flux on other edges in the domain can be derived similarly. If B_1B_2 is located on the Dirichlet boundary, we obtain directly from (10)

$$\int_{B_1B_2} \boldsymbol{F}\cdot\boldsymbol{n}_B \,\mathrm{d}s \simeq -\frac{K_B^{(n)}}{h_B^{(1)}|B_1B_2|}[(\overrightarrow{B_2O_B}\cdot\overrightarrow{B_2B_1})g_{\mathrm{D}}(B_1)+(\overrightarrow{B_1O_B}\cdot\overrightarrow{B_1B_2})g_{\mathrm{D}}(B_2)-|B_1B_2|^2u_B]$$

$$-[g_{\mathrm{D}}(B_2)-g_{\mathrm{D}}(B_1)]K_B^{(t)}, \tag{11}$$

where $g_{\mathrm{D}}(B_1)$ and $g_{\mathrm{D}}(B_2)$ are the values of Dirichlet boundary function $g_{\mathrm{D}}(x)$ at the vertex B_1 and B_2, respectively.

Finally, we can conclude that the discrete flux across an edge B_1B_2 is then

$$\int_{B_1B_2} \boldsymbol{F}\cdot\boldsymbol{n}_B \,\mathrm{d}s \simeq \begin{cases} \text{formula (10)} & \text{if } B_1B_2 \text{ is an interior edge,} \\ \text{formula (11)} & \text{if } B_1B_2 \text{ is located on } \Gamma_{\mathrm{D}}, \\ \displaystyle\int_{B_1B_2} g_{\mathrm{N}}\,\mathrm{d}s & \text{if } B_1B_2 \text{ is located on } \Gamma_{\mathrm{N}}. \end{cases} \tag{12}$$

Remark 2.1

The characteristic about the derivation here is that it is conducted according to the linearity-preserving criterion. In a structured quadrilateral mesh, the expression of the flux, given by (10), will result in a nine-point scheme with five cell-centered unknowns and four vertex unknowns. The expression for the flux (10) has some relationship with some other existing schemes:

- The tangential term in $\mathscr{D}_{AB}^{(1)}$ disappears if K is isotropic. In this case, the expression for the flux is identical to that in [7, 11, 14, 15, 22];
- If $K_A = K_B = K_{B_1B_2}$ with $K_{B_1B_2}$ is a suitably defined mean diffusion tensor on B_1B_2, the expression for the discrete flux (10) leads to that in [13]. In addition, (10) is equivalent to formula (8) in [23] by some tedious calculus, but [23] is contributed to a cell-vertex scheme in which the vertex unknowns are involved, whereas in this paper a cell-centered scheme will be given by eliminating the vertex unknowns in (10).

Copyright © 2010 John Wiley & Sons, Ltd.

DOI: 10.1002/fld

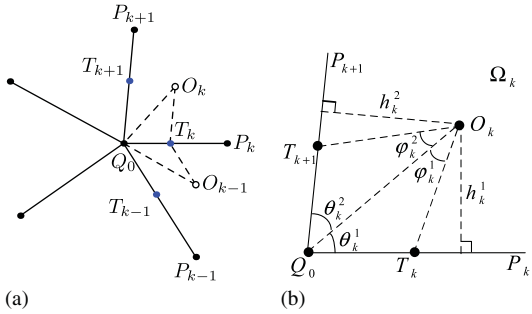

Figure 2. Notations around an interior vertex Q_0.

The vertex unknown in the discrete flux (12) will be eliminated by expressing it as a linear combination of the neighboring cell-centered unknowns, which will be discussed in the subsequent subsections. The accurate treatment for the vertex unknown is very important since it has a great influence on our new scheme.

2.2. The treatments for the interior vertex unknowns

As mentioned before, the vertex unknown is often expressed as a linear weighted combination of the neighboring cell-centered unknowns, this section is devoted to the study of the weights for the interior vertex unknowns, whereas the treatments for boundary vertex unknowns will be given in Section 2.3.

As shown in Figure 2(a), a vertex unknown can be expressed as

$$u_0 = \sum_{k=1}^{\mathcal{N}(Q_0)} \omega_k u_k,$$

where u_0 is the vertex unknown at the vertex Q_0 which is surrounded by cells Ω_k, $\mathcal{N}(Q_0)$ is the number of cells sharing the vertex Q_0, u_k is the value of u at the center O_k of the cell Ω_k which is enclosed by cell edges Q_0P_k and Q_0P_{k+1} and ω_k is known as the weight of the vertex unknown Q_0.

2.2.1. The first type of new weights with explicit expressions. As depicted in Figure 2, T_k is a dynamic point on the edge Q_0P_k, defined by

$$T_k = \tau(Q_0,k)Q_0 + [1-\tau(Q_0,k)]P_k, \quad k=1,\ldots,\mathcal{N}(Q_0), \tag{13}$$

where $\tau(Q_0,k)(0<\tau(Q_0,k)<1)$ is a dynamic parameter, depends on Q_0 and the edges sharing Q_0. $\bar{u}_k$ is the unknowns defined at T_k, Let h_k^1, h_k^2 be the distances from O_k to Q_0P_k, Q_0P_{k+1}, respectively. The rest notations θ_k^1, θ_k^2, φ_k^1, φ_k^2 are depicted in Figure 2(b).

For simplicity of exposition, we define

$$K_k = K(x_{O_k}, y_{O_k}), \quad \eta_k^1 = \frac{|Q_0T_k|}{h_k^1}, \quad \eta_k^2 = \frac{|Q_0T_{k+1}|}{h_k^2}.$$

We shall also employ a periodic numbering for the cells and vertices such as $P_{\mathcal{N}(Q_0)+1} = P_1$, $P_0 = P_{\mathcal{N}(Q_0)}$, $T_0 = T_{\mathcal{N}(Q_0)}$, etc. Moreover, in the following discussion, we shall only consider the case where $\tau(Q_0,k) = \tau(Q_0)$, i.e. the dynamic parameter depends only on Q_0 and assumes the same value on the edges sharing Q_0. Besides, we shall drop (Q_0) and simply use τ whenever there is no ambiguity.

Now, using Lemma 2.1 on the triangle domain $\triangle O_kQ_0T_k$, we have

$$\nabla u \simeq \frac{\bar{u}_k - u_0}{|Q_0T_k|^2}\overrightarrow{Q_0T_k} + \frac{\mathscr{R}\overrightarrow{Q_0T_k}}{|Q_0T_k|^2}[(u_0-u_k)\cdot\angle Q_0T_kO_k + (\bar{u}_k-u_k)\cot\angle O_kQ_0T_k],$$

Copyright © 2010 John Wiley & Sons, Ltd.

DOI: 10.1002/fld

which leads to

$$\mathbf{F}\cdot(\mathscr{R}\overrightarrow{Q_0T_k})\simeq K_k^{(n),1}\eta_k^1(u_k-u_0)-(K_k^{(t),1}+\cot\theta_k^1K_k^{(n),1})(\bar{u}_k-u_0), \tag{14}$$

where for $\alpha=1,2,\ldots,\mathscr{N}(Q_0)$,

$$K_\alpha^{(n),i}=\frac{(\mathscr{R}\overrightarrow{Q_0T_{\alpha+i-1}})^{\mathrm{T}}K_\alpha(\mathscr{R}\overrightarrow{Q_0T_{\alpha+i-1}})}{|Q_0T_{\alpha+i-1}|^2},\quad K_\alpha^{(t),i}=\frac{(\mathscr{R}\overrightarrow{Q_0T_{\alpha+i-1}})^{\mathrm{T}}K_\alpha\overrightarrow{Q_0T_{\alpha+i-1}}}{|Q_0T_{\alpha+i-1}|^2},\quad i=1,2.$$

Similarly, on the triangle $\triangle O_{k-1}T_kQ_0$,

$$\mathbf{F}\cdot(\mathscr{R}\overrightarrow{T_kQ_0})\simeq K_{k-1}^{(n),2}\eta_{k-1}^2(u_{k-1}-u_0)+(K_{k-1}^{(t),2}-\cot\theta_{k-1}^2K_{k-1}^{(n),2})(\bar{u}_k-u_0).$$

Motivated by Chen *et al*. [19], we employ the flux continuity condition across the common edge of the triangles $\triangle O_kQ_0T_k$ and $\triangle O_{k-1}T_kQ_0$, i.e.

$$\mathbf{F}\cdot(\mathscr{R}\overrightarrow{Q_0T_k})+\mathbf{F}\cdot(\mathscr{R}\overrightarrow{T_kQ_0})=0 \tag{15}$$

and through some algebra to obtain

$$\bar{u}_k-u_0=\frac{K_k^{(n),1}\eta_k^1(u_k-u_0)+K_{k-1}^{(n),2}\eta_{k-1}^2(u_{k-1}-u_0)}{K_{k-1}^{(n),2}\cot\theta_{k-1}^2+K_k^{(n),1}\cot\theta_k^1-K_{k-1}^{(t),2}+K_k^{(t),1}}. \tag{16}$$

At the present stage, we have obtained $\mathscr{N}(Q_0)$ equations for $\bar{u}_k(k=1,\ldots,\mathscr{N}(Q_0))$ and u_0. In order to eliminate all the intermediate unknowns, we should derive one more equation by the linearity-preserving criterion. When the solution is a piecewise linear function and the diffusion tensor is constant, the contour integrations of the normal component of the flux along the boundaries of quadrilateral subcells $Q_0T_kO_kT_{k+1}$, $k=1,\ldots,\mathscr{N}(Q_0)$ are all zero. Hence, by using the flux continuity condition (15), we obtain

$$\sum_{k=1}^{\mathscr{N}(Q_0)}[\mathbf{F}\cdot(\mathscr{R}\overrightarrow{T_kO_k})+\mathbf{F}\cdot(\mathscr{R}\overrightarrow{O_{k-1}T_k})]\simeq 0. \tag{17}$$

Similar to the derivation of (14), we have

$$\mathbf{F}\cdot(\mathscr{R}\overrightarrow{T_kO_k})\simeq(\bar{u}_k-u_0)[\tilde{K}_k^{(t),1}-\tilde{K}_k^{(n),1}\cot\varphi_k^1]+(u_k-u_0)[\tilde{K}_k^{(n),1}\cot(\theta_k^1+\varphi_k^1)-\tilde{K}_k^{(t),1}]$$

and

$$\begin{aligned}\mathbf{F}\cdot(\mathscr{R}\overrightarrow{O_{k-1}T_k})\simeq{}&(u_{k-1}-u_0)[\tilde{K}_{k-1}^{(t),2}+\tilde{K}_{k-1}^{(n),2}\cot(\theta_{k-1}^2+\varphi_{k-1}^2)]\\&-(\bar{u}_k-u_0)[\tilde{K}_{k-1}^{(t),2}+\tilde{K}_{k-1}^{(n),2}\cot\varphi_{k-1}^2],\end{aligned}$$

where in the cell Ω_α, $\alpha=1,2,\ldots,\mathscr{N}(Q_0)$, we define

$$\tilde{K}_\alpha^{(n),i+1}=\frac{(\mathscr{R}\overrightarrow{T_{\alpha+i}O_\alpha})^{\mathrm{T}}K_\alpha(\mathscr{R}\overrightarrow{T_{\alpha+i}O_\alpha})}{|T_{\alpha+i}O_\alpha|^2},\quad \tilde{K}_\alpha^{(t),i+1}=\frac{(\mathscr{R}\overrightarrow{T_{\alpha+i}O_\alpha})^{\mathrm{T}}K_\alpha\overrightarrow{T_{\alpha+i}O_\alpha}}{|T_{\alpha+i}O_\alpha|^2},\quad i=0,1.$$

From (17), the $(\mathscr{N}(Q_0)+1)$th equation follows,

$$\begin{aligned}&\sum_{k=1}^{\mathscr{N}(Q_0)}[\tilde{K}_{k-1}^{(n),2}\cot\varphi_{k-1}^2+\tilde{K}_k^{(n),1}\cot\varphi_k^1+\tilde{K}_{k-1}^{(t),2}-\tilde{K}_k^{(t),1}](\bar{u}_k-u_0)\\&-\left[\sum_{i=1}^{2}\tilde{K}_k^{(n),i}\cot(\theta_k^i+\varphi_k^i)-\tilde{K}_k^{(t),1}+\tilde{K}_k^{(t),2}\right](u_k-u_0)\simeq 0.\end{aligned} \tag{18}$$

Substituting (16) into the above equation and setting

$$\lambda_k=K_k^{(n),1}\eta_k^1\phi(k)+K_k^{(n),2}\eta_k^2\phi(k+1)-\sum_{i=1}^{2}\tilde{K}_k^{(n),i}\cot(\theta_k^i+\varphi_k^i)+\tilde{K}_k^{(t),1}-\tilde{K}_k^{(t),2} \tag{19}$$

Copyright © 2010 John Wiley & Sons, Ltd.

DOI: 10.1002/fld

with

$$\phi(k)=\frac{\tilde{K}_{k-1}^{(n),2}\cot\varphi_{k-1}^{2}+\tilde{K}_{k}^{(n),1}\cot\varphi_{k}^{1}+\tilde{K}_{k-1}^{(t),2}-\tilde{K}_{k}^{(t),1}}{K_{k-1}^{(n),2}\cot\theta_{k-1}^{2}+K_{k}^{(n),1}\cot\theta_{k}^{1}-K_{k-1}^{(t),2}+K_{k}^{(t),1}}, \tag{20}$$

we arrive at

$$\sum_{k=1}^{\mathcal{N}(Q_0)}\lambda_k(u_k-u_0)\simeq 0,$$

thus we obtain the new weights as follows:

$$\omega_k=\frac{\lambda_k}{\sum_{k=1}^{\mathcal{N}(Q_0)}\lambda_k}. \tag{21}$$

2.2.2. The second type of new weights with explicit expressions. In the above derivation, we have seen that the $(\mathcal{N}(Q_0)+1)$th equation (18), which plays an important role in determining the new weights, stems from the contour integration relation (17). By choosing a different contour, we can obtain another type of new weights with explicit expressions. In fact, when the solution is a piecewise linear function and the diffusion coefficient is a constant tensor, the contour integration of the normal component of the flux along the boundaries of triangles $Q_0T_kT_{k+1}(k=1,2,\ldots,\mathcal{N}(Q_0))$ vanish. Hence, by using the flux continuity condition (15), we have the contour integration relation as follows:

$$\sum_{k=1}^{\mathcal{N}(Q_0)}\mathbf{F}\cdot(\mathscr{R}\overrightarrow{T_kT_{k+1}})\simeq 0. \tag{22}$$

Applying Lemma 2.1 on the triangle $Q_0T_kT_{k+1}$ yields

$$\mathbf{F}\cdot\mathscr{R}(\overrightarrow{T_kT_{k+1}})\simeq(\overline{K}_k^{(t)}-\overline{K}_k^{(n)}\cot\vartheta_k^2)(\bar{u}_k-u_0)-(\overline{K}_k^{(t)}+\overline{K}_k^{(n)}\cot\vartheta_k^1)(\bar{u}_{k+1}-u_0), \tag{23}$$

where $\vartheta_k^1=\angle Q_0T_kT_{k+1}$, $\vartheta_k^2=\angle Q_0T_{k+1}T_k$ and in the cell Ω_α, $\alpha=1,\ldots,\mathcal{N}(Q_0)$,

$$\overline{K}_\alpha^{(n)}=\frac{(\mathscr{R}\overrightarrow{T_\alpha T_{\alpha+1}})^{\mathrm{T}}K_\alpha(\mathscr{R}\overrightarrow{T_\alpha T_{\alpha+1}})}{|T_\alpha T_{\alpha+1}|^2},\quad \overline{K}_\alpha^{(t)}=\frac{(\mathscr{R}\overrightarrow{T_\alpha T_{\alpha+1}})^{\mathrm{T}}K_\alpha\overrightarrow{T_\alpha T_{\alpha+1}}}{|T_\alpha T_{\alpha+1}|^2}.$$

Substituting (23) into (22), we obtain

$$\sum_{k=1}^{\mathcal{N}(Q_0)}[\overline{K}_{k-1}^{(t)}-\overline{K}_k^{(t)}+\overline{K}_{k-1}^{(n)}\cot\vartheta_{k-1}^1+\overline{K}_k^{(n)}\cot\vartheta_k^2](\bar{u}_k-u_0)\simeq 0. \tag{24}$$

By substituting (16) into (24), we reach

$$\sum_{k=1}^{\mathcal{N}(Q_0)}\bar{\lambda}_k(u_k-u_0)\simeq 0,$$

where

$$\bar{\lambda}_k=K_k^{(n),1}\eta_k^1\zeta(k)+K_k^{(n),2}\eta_k^2\zeta(k+1), \tag{25}$$

and

$$\zeta(k)=\frac{\overline{K}_{k-1}^{(n)}\cot\vartheta_{k-1}^1+\overline{K}_k^{(n)}\cot\vartheta_k^2+\overline{K}_{k-1}^{(t)}-\overline{K}_k^{(t)}}{K_{k-1}^{(n),2}\cot\theta_{k-1}^2+K_k^{(n),1}\cot\theta_k^1-K_{k-1}^{(t),2}+K_k^{(t),1}}. \tag{26}$$

Hence, we obtain another type of new weights

$$w_k=\frac{\bar{\lambda}_k}{\sum_{k=1}^{\mathcal{N}(Q_0)}\bar{\lambda}_k}. \tag{27}$$

Copyright © 2010 John Wiley & Sons, Ltd.

DOI: 10.1002/fld

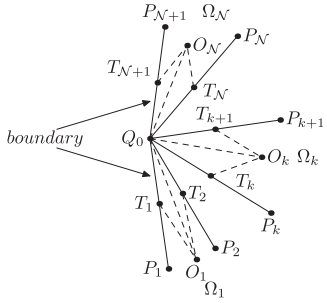

Figure 3. Notations around a boundary vertex Q_0.

Finally, we conclude this subsection by the following remark.

Remark 2.2
The new weights defined by (21) and (19) are dependent on the parameter τ in (13) whereas the new weights defined by (27) and (25) are independent of τ.

2.3. The treatments for the boundary vertex unknowns

In this subsection, we will explain how the boundary vertex value depends on the approximate cell-centered unknowns. If one vertex Q_0 is a Dirichlet boundary vertex, one can simply set $u_0 = g_{\mathrm{D}}(Q_0)$. In the following context, we will focus on the treatment for the Neumann boundary conditions. The discretization of the Robin boundary conditions can be done similarly. We point out that the treatment for boundary vertex unknowns in this paper has no essential difference with that for interior vertex unknowns in Section 2.2.

We assume that vertex Q_0 is located on a Neumann boundary Γ_{N} and define a local numbering for the cells and edges which are connected to Q_0 (Figure 3). Q_0 is surrounded by $\mathcal{N}$ cells, therefore there are $\mathcal{N}+1$ edges, the first and last edges are located on the boundary. By using the definition of the flux in (2), we can rewrite (1c) as:

$$\mathbf{F}\cdot\mathbf{n} = g_{\mathrm{N}} \quad \text{on}\,\Gamma_{\mathrm{N}}.$$

First, by using the flux continuity across the cell edge Q_0P_k, we obtain (16) with $k = 2, \ldots, \mathcal{N}$. Second, by applying Lemma 2.1 on the triangle domain $\triangle O_1 Q_0 T_1$ and $\triangle O_{\mathcal{N}} T_{\mathcal{N}+1} Q_0$, respectively, we get

$$\bar{u}_1 - u_0 \simeq \frac{K_1^{(n)}\eta_1^1(u_1-u_0) - |Q_0T_1|g_{\mathrm{N}}(T_1)}{K_1^{(t)} + K_1^{(n)}\cot\theta_1^1}, \tag{28}$$

$$\bar{u}_{\mathcal{N}+1} - u_0 \simeq \frac{K_{\mathcal{N}}^{(n)}\eta_{\mathcal{N}}^2(u_{\mathcal{N}}-u_0) - |Q_0T_{\mathcal{N}+1}|g_{\mathrm{N}}(T_{\mathcal{N}+1})}{K_{\mathcal{N}}^{(n)}\cot\theta_{\mathcal{N}}^2 - K_{\mathcal{N}}^{(t)}}, \tag{29}$$

where $g_{\mathrm{N}}(T_1)$ and $g_{\mathrm{N}}(T_{\mathcal{N}+1})$ denote the values of g_{N} at T_1 and $T_{\mathcal{N}+1}$, respectively.

Finally, the last equation can be obtained in a way which is similar to that of (18). By choosing the contour $Q_0 \to T_1 \to O_1 \to \cdots \to T_k \to O_k \to \cdots \to T_{\mathcal{N}+1} \to Q_0$, we obtain

$$\sum_{k=1}^{\mathcal{N}} [\mathbf{F}\cdot(\mathscr{R}\overrightarrow{T_kO_k}) + \mathbf{F}\cdot(\mathscr{R}\overrightarrow{O_kT_{k+1}})] + \mathbf{F}\cdot(\mathscr{R}\overrightarrow{Q_0T_1}) + \mathbf{F}\cdot(\mathscr{R}\overrightarrow{T_{\mathcal{N}+1}Q_0}) \simeq 0.$$

Copyright © 2010 John Wiley & Sons, Ltd.

DOI: 10.1002/fld

By Lemma 2.1, we have

$$\sum_{k=1}^{\mathscr{N}}\{(\bar{u}_k-u_0)[\tilde{K}_k^{(t),1}-\tilde{K}_k^{(n),1}\cot\varphi_k^1]-(\bar{u}_{k+1}-u_0)[\tilde{K}_k^{(n),2}\cot\varphi_k^2+\tilde{K}_k^{(t),2}]\}$$
$$+\sum_{k=1}^{\mathscr{N}}[\tilde{K}_k^{(n),1}\cot(\theta_k^1+\varphi_k^1)+\tilde{K}_k^{(n),2}\cot(\theta_k^2+\varphi_k^2)-\tilde{K}_k^{(t),1}+\tilde{K}_k^{(t),2}](u_k-u_0)$$
$$+|Q_0T_1|g_{\mathrm{N}}(T_1)+|Q_0T_{\mathscr{N}+1}|g_{\mathrm{N}}(T_{\mathscr{N}+1})\simeq 0.$$

Substituting (16), (28) and (29) into the above equation, we get the first type of explicit weights for the boundary vertex unknown u_0

$$u_0\simeq\left(\sum_{k=1}^{\mathscr{N}}\lambda_k\right)^{-1}\left\{\sum_{k=1}^{\mathscr{N}}\lambda_k u_k-\sum_{j=1,\mathscr{N}+1}[1+\phi(j)]|Q_0T_j|g_{\mathrm{N}}(T_j)\right\},\tag{30}$$

where λ_k was defined by (19) and

$$\phi(k)=\begin{cases}\dfrac{\tilde{K}_1^{(n),1}\cot\varphi_1^1-\tilde{K}_1^{(t),1}}{K_1^{(n)}\cot\theta_1^1+K_1^{(t)}}, & k=1;\\ \text{formula (20)}, & 2\leqslant k\leqslant\mathscr{N};\\ \dfrac{\tilde{K}_{\mathscr{N}}^{(n),2}\cot\varphi_{\mathscr{N}}^2+\tilde{K}_{\mathscr{N}}^{(t),2}}{K_{\mathscr{N}}^{(n)}\cot\theta_{\mathscr{N}}^2-K_{\mathscr{N}}^{(t)}}, & k=\mathscr{N}+1.\end{cases}$$

We can also choose another contour as $Q_0\to T_1\to\cdots\to T_k\to\cdots\to T_{\mathscr{N}+1}\to Q_0$ and get

$$\sum_{k=1}^{\mathscr{N}}[(\overline{K}_k^{(t)}-\overline{K}_k^{(n)}\cot\vartheta_k^2)(\bar{u}_k-u_0)-(\overline{K}_k^{(t)}+\overline{K}_k^{(n)}\cot\vartheta_k^1)(\bar{u}_{k+1}-u_0)]$$
$$+|Q_0T_1|g_{\mathrm{N}}(T_1)+|Q_0T_{\mathscr{N}+1}|g_{\mathrm{N}}(T_{\mathscr{N}+1})\simeq 0.$$

Substituting (16), (28) and (29) into the above equation, we get another type of explicit weights for the boundary vertex u_0

$$u_0\simeq\left(\sum_{k=1}^{\mathscr{N}}\bar{\lambda}_k\right)^{-1}\left[\sum_{k=1}^{\mathscr{N}}\bar{\lambda}_k u_k-\sum_{j=1,\mathscr{N}+1}[1+\zeta(j)]|Q_0T_j|g_{\mathrm{N}}(T_j)\right],\tag{31}$$

where $\bar{\lambda}_k$ is defined by (25) and

$$\zeta(k)=\begin{cases}\dfrac{\overline{K}_1^{(n)}\cot\vartheta_1^2-\overline{K}_1^{(t)}}{K_1^{(n)}\cot\theta_1^1+K_1^{(t)}}, & k=1;\\ \text{formula (26)}, & 2\leqslant k\leqslant\mathscr{N};\\ \dfrac{\overline{K}_{\mathscr{N}}^{(n)}\cot\vartheta_{\mathscr{N}}^1+\overline{K}_{\mathscr{N}}^{(t)}}{K_{\mathscr{N}}^{(n)}\cot\theta_{\mathscr{N}}^2-K_{\mathscr{N}}^{(t)}}, & k=\mathscr{N}+1.\end{cases}$$

3. NUMERICAL EXAMPLES

In this section, we present some numerical results to demonstrate the accuracy and the efficiency of the linearity-preserving cell-centered scheme on various mesh families.

Copyright © 2010 John Wiley & Sons, Ltd.

DOI: 10.1002/fld

Table I. The notations for the various schemes used in the numerical computation.

Notation	Algorithm description
LPEW1	The linearity-preserving cell-centered scheme with weights given by (21)
LPEW2	The linearity-preserving cell-centered scheme with weights given by (27)
MPFA	The MPFA O-method suggested in [17] and analyzed in [18]
GMPFA	The generalized MPFA scheme with $\tau=0.4$ [15]
MFEM	The lowest-order Raviart–Thomas mixed finite element method

Table II. Summary of all numerical tests with the description of the features of the diffusion tensor K (continuity (cont.), symmetry (sym.) and anisotropy), types of boundary conditions, and the considered meshes: Mesh1–Mesh6 (Figure 4), Mesh7 (Figure 6), Mesh8 (Figure 15).

	Features of diffusion tensor				
No.	Cont.	Sym.	Anisotropy	Boundary condition	Meshes
Test 1	Yes	Yes	Mild	D	Mesh1–Mesh6
Test 2	No	Yes	Mild	D	Mesh1, Mesh4, Mesh7
Test 3	Yes	No	Righi–Leduc	D–N	Mesh1, Mesh4, Mesh7
Test 4	Yes	Yes	Strong	D	Mesh8
Test 5	Yes	Yes	Strong	D, D-N, N	Mesh1

'D' and 'N' are the abbreviations for the Dirichlet and Neumann boundary condition respectively.

The notations of the algorithms used in this section are shown in Table I and the numerical tests are summarized in Table II. Test 1 is used to validate the discrete maximum principle and compare the convergence rates of the four schemes (LPEW1, LPEW2, MPFA and GMPFA) on a regular triangular mesh and then on some distorted meshes, and then the good performance of our scheme on nonconforming meshes is also given. Test 2 confirms the optimal accuracy of our scheme for the case of discontinuous diffusion tensor and highly distorted quadrilateral meshes, whereas Test 3 verifies that for a nonsymmetric tensor of Righi–Leduc-type and highly distorted quadrilateral meshes. Test 4 is utilized to discuss the non-physical oscillations, the discrete maximum principle, the convergence rates of the schemes (LPEW1, LPEW2, MPFA and MFEM) for the case of heterogeneous rotating anisotropy and large magnitude of the sink source terms. Test 5 is employed to investigate the numerical locking phenomenon for our new scheme in case of three conditions: Dirichlet, mixed Dirichlet–Neumann and nearly pure Neumann boundary conditions.

All tests presented in this section have an analytical solution, so the solution errors and edge normal flux errors are investigated in the discrete L^2 norms, which are defined as in [24] by the following expressions:

$$E_u(h)=\left(\sum_i S_i(u_{h,i}-u_i)^2\right)^{1/2},$$

$$E_q(h)=\left(\sum_j Q_j(q_{h,j}-q_j)^2/\sum_j Q_j\right)^{1/2},$$

where S_i is the area of mesh cell i, Q_j is the volume associated with edge j (equal to the sum of the areas of the two cells separated by the edge j). Further, $q=-K\nabla u\cdot\boldsymbol{n}$ is the edge normal flux density. Subscript h refers to the discrete solution. The analytical solution u_i is computed at the center of the cell i, whereas the analytical flux q_j of cell edge j is evaluated by the mid-point rule.

Copyright © 2010 John Wiley & Sons, Ltd.

DOI: 10.1002/fld

The rate of convergence can be obtained by a least squares fit on the ones computed on each two successive meshes by the following formula:

$$R_\alpha = \frac{\log[E_\alpha(h_2)/E_\alpha(h_1)]}{\log(h_2/h_1)}, \quad \alpha = u, q,$$

where h_1, h_2 denote the mesh sizes of the two successive meshes, and $E_\alpha(h_1)$, $E_\alpha(h_2)$ the corresponding L_2 errors of the solution or edge normal flux.

In addition, we use the following notations for the numerical tests:

- `umin`: value of the minimum of the approximate solution;
- `umax`: value of the maximum of the approximate solution.

3.1. *Test 1*: *mild anisotropy*

We consider the problem (1a) with full Dirichlet boundary condition (1b) and $\Omega = [0,1]^2$. A homogeneous anisotropic tensor and the exact solution are given below:

$$K = \begin{pmatrix} 1.5 & 0.5 \\ 0.5 & 1.5 \end{pmatrix}, \quad u(x,y) = \frac{1}{2}\left[\frac{\sin((1-x)(1-y))}{\sin(1)} + (1-x)^3(1-y)^2\right],$$

where the exact solution is located in the interval [0,1]. This numerical test is classical, and can be found in [25] as a benchmark with a slight modification for the exact solution.

We use a sequence of the strictly acute triangular mesh (Mesh1), two distorted quadrilateral meshes (Mesh2 and Mesh3), randomly perturbed quadrilateral mesh (Mesh4), a locally refined nonconforming rectangular mesh (Mesh5) and a nonmatching random mesh (Mesh6) in this numerical test (Figure 4), and the mesh refinement levels used for L^2 norm computation are also given in Figure 4.

First, in Table III, we give the comparison of our linearity-preserving cell-centered schemes LPEW1 and LPEW2 with schemes MPFA and GMPFA on the first four meshes Mesh1–Mesh4. Table III shows the following:

- The minimum and maximum solutions are obtained on the coarse meshes, which are exactly those in Figure 4(a)–4(d), and we can see that the four schemes satisfy the discrete maximum principle in this test.
- All schemes show a second-order convergence rate with respect to the L^2 norm of the solution on the four types of meshes except that the convergence rate of GMPFA is about $h^{1.4}$ on Mesh4.
- All schemes have more than first-order convergence rate with respect to the L^2 norm of the edge normal flux except schemes MPFA and GMPFA on Mesh4.

Second, we employ two types of nonmatching meshes (Mesh5 and Mesh6) to see how the proposed schemes LPEW1 and LPEW2 behave.

The convergence rates for the solution and edge normal flux errors are graphically depicted in Figure 5 as log–log plots of the discrete L^2 norm errors versus the characteristic mesh size h. The actual convergence order is reflected by the slopes of the experimental error curves. On Mesh5, the convergence rates of LPEW1 and LPEW2 for the solution errors and edge normal flux errors are about h^2 and $h^{1.5}$, respectively, and the convergence rates of LPEW1 and LPEW2 are around h^2 for the solution errors and $h^{1.3}$ for edge normal flux errors on Mesh6.

Finally, all the simulations demonstrate that LPEW1 and LPEW2 have desirable convergence for the solution and flux errors on the triangular or distorted quadrilateral (possibly nonconforming) meshes.

3.2. *Test 2*: *discontinuous anisotropy*

In this section, we investigate the convergence of our method for a problem with a discontinuous diffusion tensor. We solve the problem (1a) with the full Dirichlet boundary condition (1b) and $\Omega = [0,1]^2$. Let the diffusion tensor K change the eigenvalues and orientation of eigenvectors

Copyright © 2010 John Wiley & Sons, Ltd.

DOI: 10.1002/fld

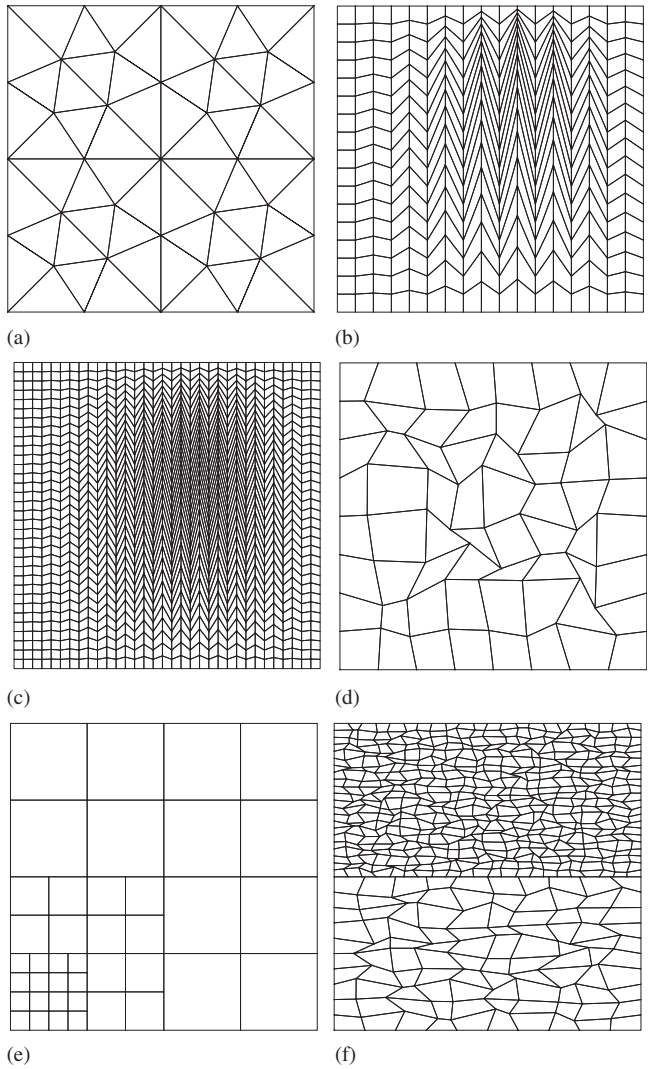

Figure 4. Samples of the meshes used for simulations: each mesh was used with five successive mesh levels, and the range of associated characteristic mesh size $h_i (i=1,\ldots,5)$ is shown in the bracket as (h_1, h_5) in the caption of each mesh: (a) Mesh1: acute triangular mesh $(2.5\times10^{-1}, 1.56\times10^{-2})$; (b) Mesh2: quadrilateral mesh $(3.29\times10^{-1}, 6.72\times10^{-2})$; (c) Mesh3: quadrilateral mesh $(1.70\times10^{-1}, 4.27\times10^{-2})$; (d) Mesh4: randomly perturbed mesh $(2.85\times10^{-1}, 1.91\times10^{-2})$; (e) Mesh5: locally refined mesh $(3.54\times10^{-1}, 2.21\times10^{-2})$; and (f) Mesh6: nonmatching random mesh $(7.60\times10^{-1}, 4.56\times10^{-2})$.

across the line $x=0.5$,

$$K=\begin{cases}\begin{pmatrix}10 & 2\\ 2 & 5\end{pmatrix}, & x\leqslant 0.5,\\ \begin{pmatrix}1 & 0\\ 0 & 1\end{pmatrix}, & x>0.5,\end{cases}$$

We choose the following exact solution:

$$u(x,y)=\begin{cases}[1+(x-0.5)(0.1+8\pi(y-0.5))]\exp(-20\pi(y-0.5)^2), & x\leqslant 0.5,\\ \exp(x-0.5)\exp(-20\pi(y-0.5)^2), & x>0.5.\end{cases}$$

This test is rebuilt from a numerical experiment in [26].

Copyright © 2010 John Wiley & Sons, Ltd.

DOI: 10.1002/fld

Table III. Test 1: minimum and maximum solutions and the convergence rates for the solution and edge normal flux errors on various meshes.

Mesh	Scheme	umin	umax	R_u	R_q
Mesh1	LPEW1	4.02×10^{-3}	7.62×10^{-1}	1.980	1.665
	LPEW2	3.99×10^{-3}	7.62×10^{-1}	1.980	1.711
	MPFA	2.81×10^{-3}	7.51×10^{-1}	2.000	1.000
	GMPFA	3.29×10^{-3}	7.57×10^{-1}	1.986	1.001
Mesh2	LPEW1	4.74×10^{-4}	9.11×10^{-1}	2.320	1.745
	LPEW2	4.80×10^{-4}	9.11×10^{-1}	1.887	1.530
	MPFA	3.15×10^{-4}	9.10×10^{-1}	2.011	1.952
	GMPFA	3.14×10^{-4}	9.10×10^{-1}	2.012	1.894
Mesh3	LPEW1	8.27×10^{-5}	9.53×10^{-1}	1.573	1.260
	LPEW2	1.32×10^{-4}	9.53×10^{-1}	1.933	1.268
	MPFA	8.88×10^{-5}	9.53×10^{-1}	1.992	1.952
	GMPFA	8.86×10^{-5}	9.53×10^{-1}	2.006	1.777
Mesh4	LPEW1	2.71×10^{-3}	8.14×10^{-1}	1.992	1.211
	LPEW2	2.63×10^{-3}	8.14×10^{-1}	2.005	1.179
	MPFA	2.19×10^{-3}	8.07×10^{-1}	1.977	0.646
	GMPFA	2.26×10^{-3}	8.09×10^{-1}	1.413	0.190

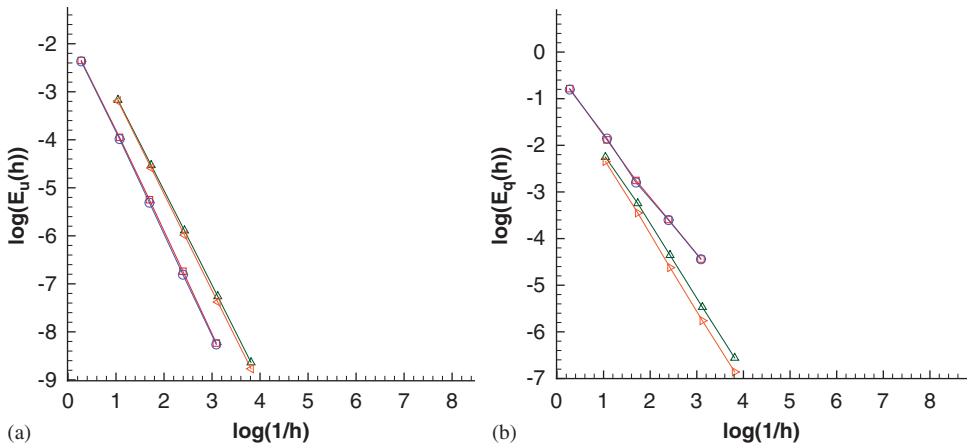

Figure 5. Test 1: L^2 errors versus mesh size h for LPEW1 and LPEW2 on Mesh5 and Mesh6 with symbols: Δ (LPEW1 on Mesh5), $\triangleright$ (LPEW2 on Mesh5), $\square$ (LPEW1 on Mesh6), $\bigcirc$ (LPEW2 on Mesh6): (a) solution and (b) edge normal flux.

The numerical tests are performed on three different mesh families: the triangular mesh (Mesh1), random mesh (Mesh4) and Shestakov mesh (Mesh7, see Figure 6), which is highly skewed and highly distorted and frequently arise from computational hydrodynamics. The convergence behaviors of the four schemes (LPEW1, LPEW2, MPFA and GMPFA) are given on the three mesh families. The solution profile is depicted in Figure 7 which has a hollow around the point (0.5,0.5).

To begin with, the convergence results on the triangular mesh (Mesh1) are displayed in Figure 8 where we notice that the convergence rates of LPEW1 and LPEW2 for the edge normal flux errors are a little better than that of schemes MPFA and GMPFA.

Second in Figures 9 and 10, we plot the convergence results on two distorted quadrilateral meshes (Mesh4 and Mesh7). We notice that LPEW1 and LPEW2 perform very well on

Copyright © 2010 John Wiley & Sons, Ltd.

DOI: 10.1002/fld

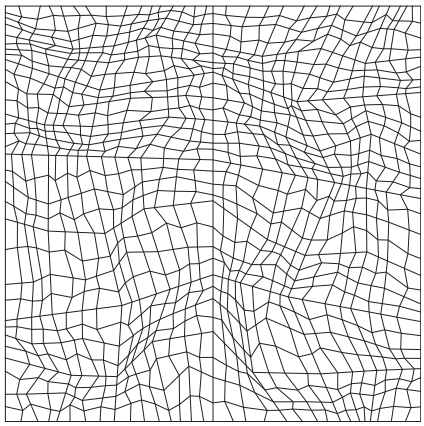

Figure 6. Mesh7: Shestakov mesh (five meshes: mesh size ranging from 3.79×10^{-1} to 8.23×10^{-2}).

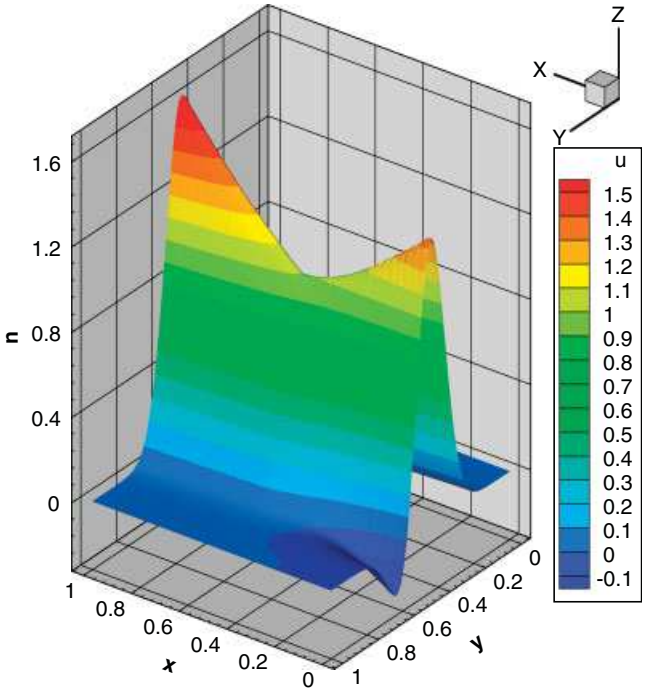

Figure 7. Solution profile for test 2.

the discontinuous case and have a comparable convergence results with schemes MPFA and GMPFA.

Finally, we ascertain that the discontinuity of the diffusion tensor does not affect the convergence rate for all the considered meshes in this test.

3.3. Test 3: *anisotropy of Righi–Leduc type*

We solve problem (1a) on a unit square domain $\Omega=(0,1)\times(0,1)$ with a tensorial conductivity of Righi-Leduc type

$$K=\begin{pmatrix} a & by \\ -by & a \end{pmatrix}$$

Copyright © 2010 John Wiley & Sons, Ltd.

DOI: 10.1002/fld

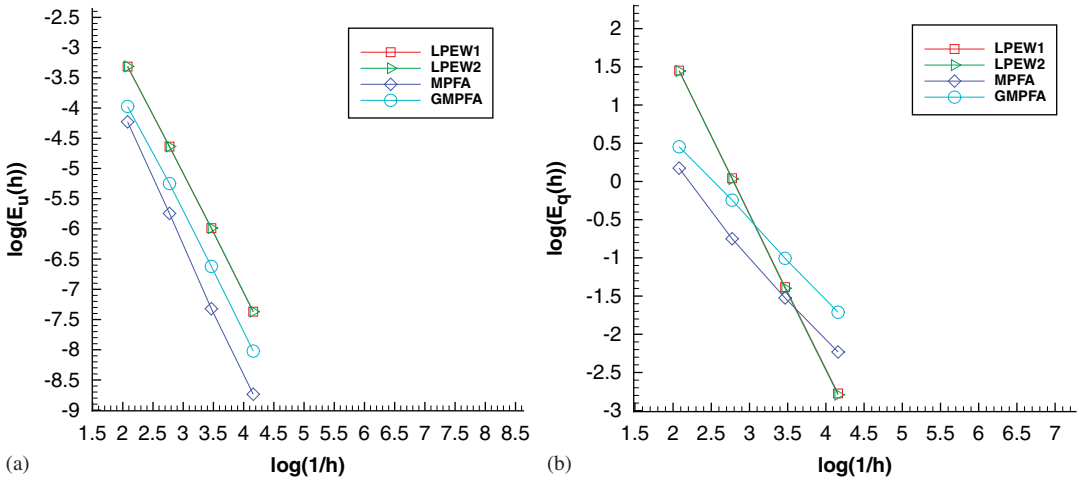

Figure 8. Test 2: L^2 errors versus mesh size h on the triangular mesh (Mesh1): (a) solution and (b) edge normal flux.

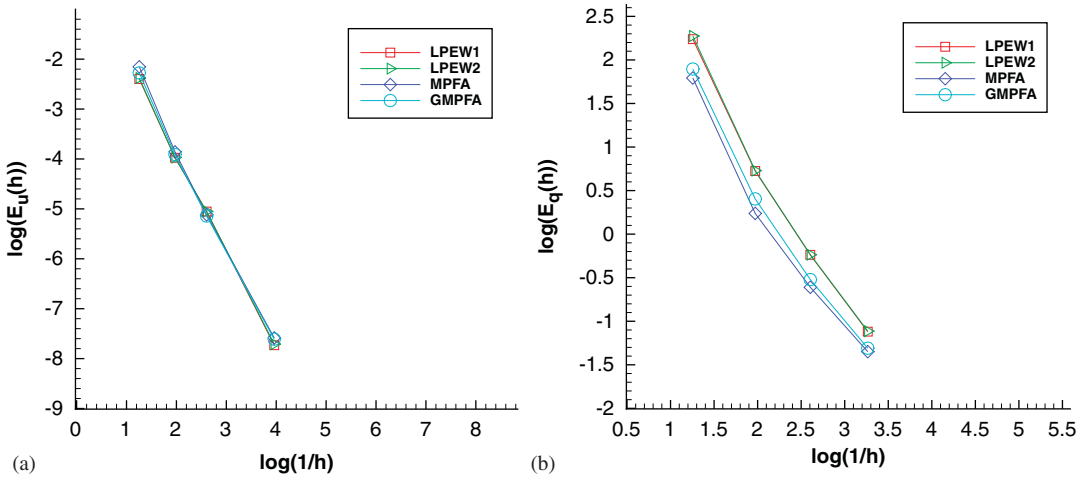

Figure 9. Test 2: L^2 errors versus mesh size h on the random mesh (Mesh4): (a) solution and (b) edge normal flux.

and the exact solution

$$u(x,y)=\frac{\exp\left(\frac{b}{a}x\right)-1}{\exp\left(\frac{b}{a}\right)-1}.$$

Here we choose $a=1$ and $b=2$. The Dirichlet boundary condition is imposed on the top side of the unit square domain and the Neumann boundary conditions on the remaining three sides.

This model is a simplified version of anisotropic electron heat transport in the presence of transverse magnetic fields, which may appear in the numerical simulation of laser-driven inertial confinement fusion [27].

Experiments are carried out on the triangular mesh (Mesh1), randomly perturbed quadrilateral mesh (Mesh4) and Shestakov mesh (Mesh7). On the above three different mesh families, the convergence behavior of the four schemes (LPEW1, LPEW2, MPFA and GMPFA) is displayed in Figures 11–13 as log–log plots. In all figures, the left plot corresponds to the error curves for the solution, and the right plot to the error curves for the approximation of the edge normal flux.

Copyright © 2010 John Wiley & Sons, Ltd.

DOI: 10.1002/fld

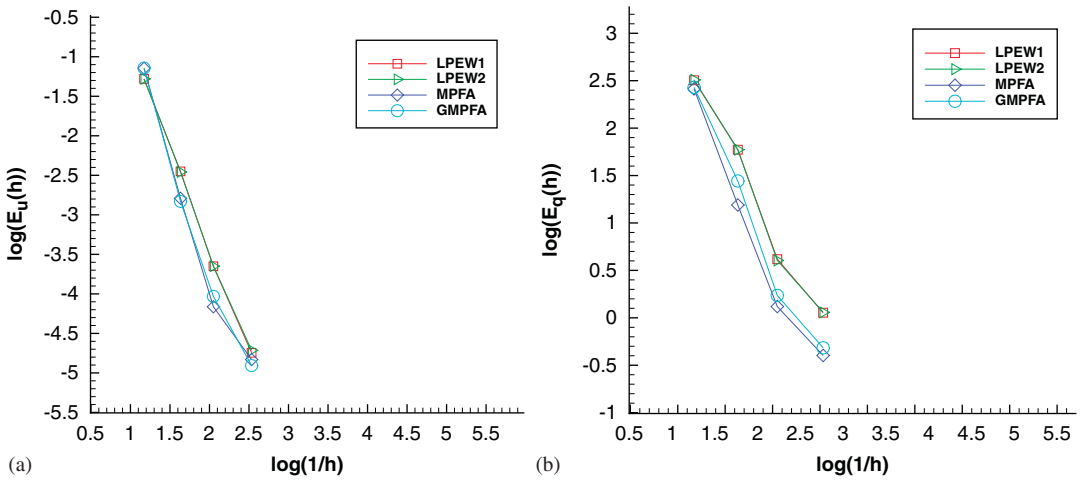

Figure 10. Test 2: L^2 errors versus mesh size h on the Shestakov mesh (Mesh7): (a) solution and (b) edge normal flux.

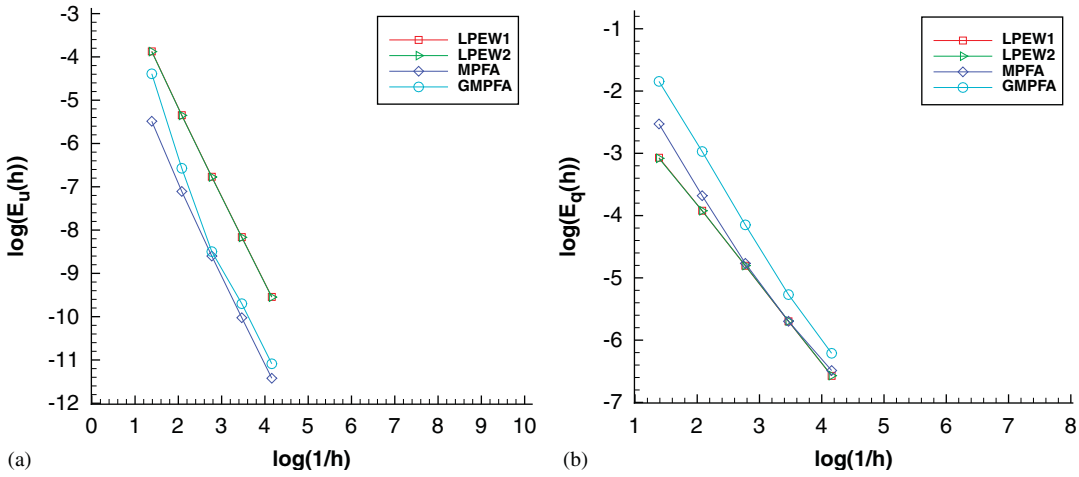

Figure 11. Test 3: L^2 errors versus mesh size h on the triangular mesh (Mesh1): (a) solution and (b) edge normal flux.

These graphs show the following:

- As shown in Figure 11, the convergence rates of the four schemes are h^2 for the solution errors and about $h^{1.2\sim1.6}$ for edge normal flux errors on the triangular mesh. The solution errors for the schemes LPEW1 and LPEW2 are bigger than that for MPFA and GMPFA, but the edge normal flux errors for LPEW1 and LPEW2 are a little smaller than that for MPFA and GMPFA.
- The convergence analysis on a sequence of randomly perturbed quadrilateral meshes is the challenging test for any discretization scheme. Figure 12(a) shows that the approximate solution is quadratically convergent in the L^2 norm and Figure 12(b) shows the expected linear convergence of the approximation of edge normal flux.
- On the Shestakov mesh (Mesh7), the convergence rates of the four schemes are around $h^{2.5}$ for the solution errors and higher than $h^{1.0}$ for edge normal flux errors (Figure 13). The solution errors of the four schemes are almost the same on the same mesh, but the edge normal flux errors for LPEW1 are about twice higher than that for the other three schemes on the finer meshes.

Copyright © 2010 John Wiley & Sons, Ltd.

DOI: 10.1002/fld

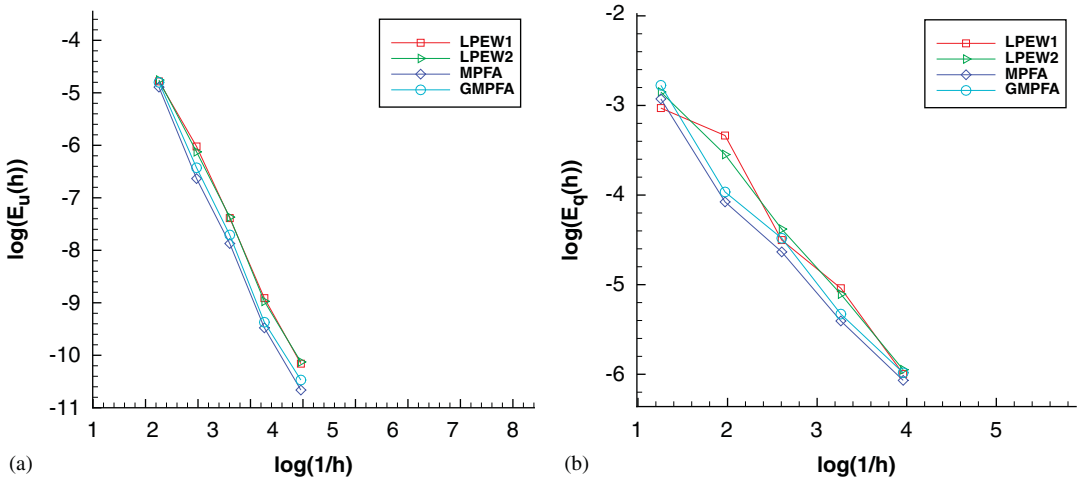

Figure 12. Test 3: L^2 errors versus mesh size h on the random mesh (Mesh4): (a) solution and (b) edge normal flux.

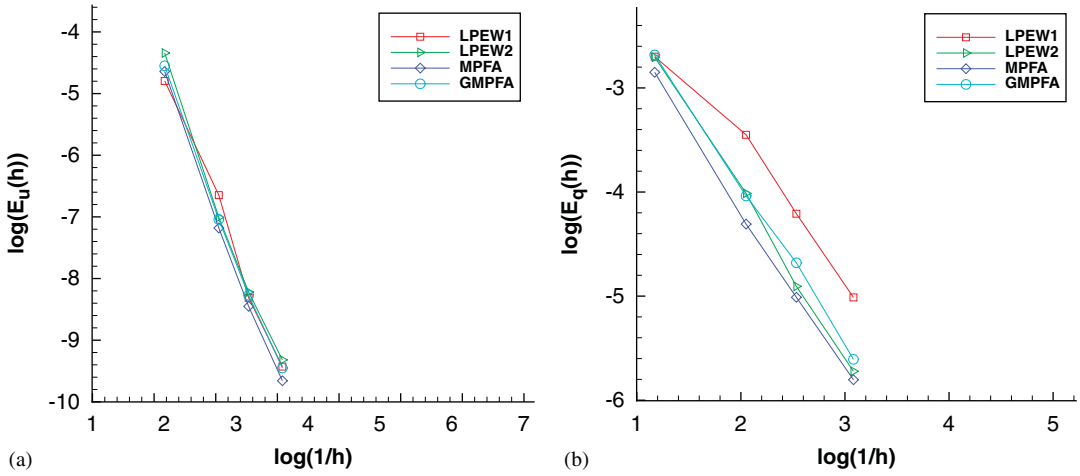

Figure 13. Test 3: L^2 errors versus mesh size h on the Shestakov mesh (Mesh7): (a) solution and (b) edge normal flux.

3.4. *Test 4*: *heterogeneous-rotating anisotropy*

In this test, problem (1a) with the full Dirichlet boundary condition (1b) is defined on a unit square domain $\Omega=[0,1]^2$ with the anisotropic and heterogeneous diffusion tensor field. The tensor coefficient is a rotating anisotropic tensor:

$$K=\begin{pmatrix}\alpha x^2+y^2 & (\alpha-1)xy\\ (\alpha-1)xy & x^2+\alpha y^2\end{pmatrix}$$

and we consider the following exact solution in this test:

$$u(x,y)=\exp[-20\pi((x-0.5)^2+(y-0.5)^2)].$$

We set $\alpha>1$ in this test. Then the eigenvalues of K are $\lambda_1(x,y)=x^2+y^2$ and $\lambda_2(x,y)=\alpha(x^2+y^2)$. The anisotropy ratio is therefore α in the whole domain, and we have $\inf_{(x,y)\in\Omega}\lambda_2=0$ and $\sup_{(x,y)\in\Omega}\lambda_2=2\alpha$, which corresponds to a highly heterogeneous case.

Copyright © 2010 John Wiley & Sons, Ltd.

DOI: 10.1002/fld

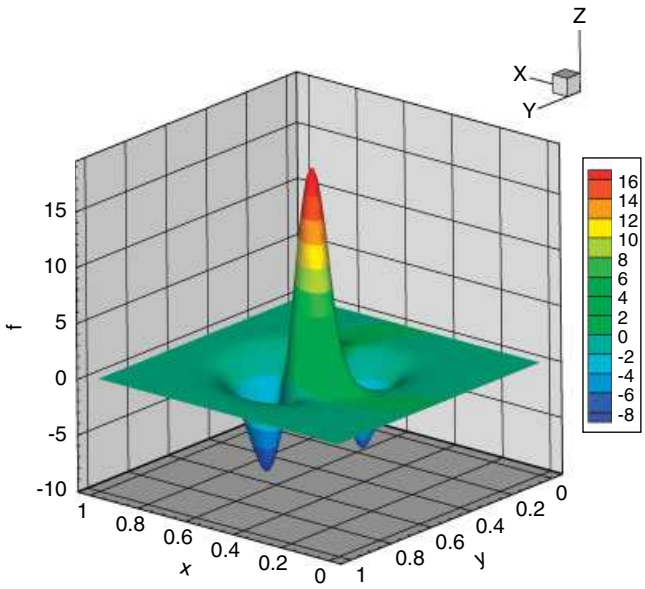

Figure 14. Test 4: The distribution of the sink source term f for $\alpha = 10^3$.

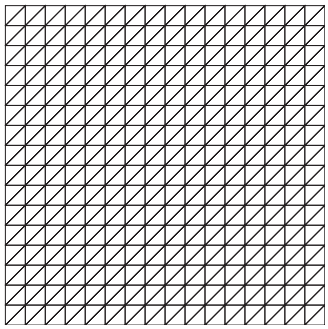

Figure 15. Mesh8: uniform triangular mesh (three meshes with mesh size $h_i = 2^{1-i} \times 8.84 \times 10^{-2}$, $i = 1, 2, 3$).

The sink source term f corresponds to an injection at the center of the domain located between two sinks, and the magnitude of the sink source term increases as α increases (Figure 14). This test is inspired from [26] and induces numerical locking for some difference schemes.

We study the behavior of the four schemes LPEW1, LPEW2, MPFA and MFEM for various anisotropy ratio α on a sequence of successively refined triangular meshes (Figure 15).

Table IV reports the minimum and maximum solutions, the solution errors and edge normal flux errors for the anisotropy ratio $\alpha = 10, 100, 1000$ on Mesh8. The results in this table reveal the following:

- In this test, MPFA shows no convergence for $\alpha = 100, 1000$ on the finer mesh with mesh size $h_3 = 2.21 \times 10^{-2}$, and LPEW1 shows no convergence for $\alpha = 1,000$ on the finer mesh. But MPFA works very well on the uniform rectangular mesh as shown in [26].
- The values of the numerical solution should be within the range [0,1]. For anisotropy $\alpha = 1,000$, MFEM gives a solution with significant oscillations ($\texttt{umin} = -4.10 \times 10^0$, $\texttt{umax} = 9.300$) on the coarse mesh (Figure 16). These oscillations can be reduced on the finer mesh ($\texttt{umin} = -1.60 \times 10^{-1}, \texttt{umax} = 1.620$).
- The non-physical oscillations are avoided or strongly reduced when using our schemes. The minimum and maximum solutions with LPEW2 are -1.55×10^{-2} and 0.986 for $\alpha = 1,000$,

Copyright © 2010 John Wiley & Sons, Ltd.

DOI: 10.1002/fld

Table IV. Comparisons of solution behaviors of various methods on the uniform triangular meshes (Mesh8) with anisotropy ratios $\alpha = 10, 100, 1000$.

	$\alpha = 10$				$\alpha = 100$				$\alpha = 1000$			
Scheme	umin	umax	E_u	E_q	umin	umax	E_u	E_q	umin	umax	E_u	E_q
LPEW1(h_1)	-1.97×10^{-3}	0.993	7.51×10^{-3}	1.28×10^{-1}	-5.08×10^{-3}	0.996	1.48×10^{-2}	1.686	-6.39×10^{-2}	1.062	4.14×10^{-2}	45.57
LPEW2(h_1)	-1.73×10^{-3}	0.989	6.98×10^{-3}	1.27×10^{-1}	-4.15×10^{-3}	0.985	1.44×10^{-2}	1.667	-1.55×10^{-2}	0.986	3.17×10^{-2}	22.97
MFEM(h_1)	-1.10×10^{-3}	0.975	2.72×10^{-2}	2.17×10^{-1}	-2.75×10^{-1}	1.727	1.28×10^{-1}	2.697	-4.10×10^{0}	9.300	1.30×10^{0}	27.89
MPFA(h_1)	-1.22×10^{-3}	0.997	8.38×10^{-3}	1.18×10^{-1}	-3.57×10^{-2}	0.972	2.50×10^{-2}	1.365	—	—	—	—
LPEW1(h_2)	-4.45×10^{-4}	0.998	1.81×10^{-3}	3.21×10^{-2}	-1.66×10^{-3}	0.999	3.48×10^{-3}	0.430	-3.26×10^{-2}	1.040	2.12×10^{-2}	21.83
LPEW2(h_2)	-3.90×10^{-4}	0.997	1.69×10^{-3}	3.18×10^{-2}	-1.28×10^{-3}	0.996	3.60×10^{-3}	0.437	-7.32×10^{-3}	0.993	1.14×10^{-2}	8.479
MFEM(h_2)	-1.96×10^{-4}	0.995	1.32×10^{-2}	5.60×10^{-2}	-1.99×10^{-2}	1.211	3.55×10^{-2}	0.699	-1.06×10^{0}	3.400	3.42×10^{-1}	9.540
MPFA(h_2)	-1.78×10^{-4}	0.999	1.99×10^{-3}	2.86×10^{-2}	-4.10×10^{-2}	0.988	1.04×10^{-2}	0.982	—	—	—	—
LPEW1(h_3)	-1.01×10^{-4}	1.000	4.48×10^{-4}	8.05×10^{-3}	-4.39×10^{-4}	1.000	8.58×10^{-4}	0.109	—	—	—	—
LPEW2(h_3)	-8.53×10^{-5}	1.000	4.20×10^{-4}	7.98×10^{-3}	-3.44×10^{-4}	1.000	9.01×10^{-4}	0.111	-2.71×10^{-3}	0.992	3.31×10^{-3}	2.596
MFEM(h_3)	-3.49×10^{-5}	0.999	6.55×10^{-3}	1.41×10^{-2}	-2.99×10^{-4}	1.055	1.06×10^{-2}	0.177	-1.60×10^{-1}	1.620	8.69×10^{-2}	3.284
MPFA(h_3)	-3.11×10^{-5}	1.000	4.90×10^{-4}	7.12×10^{-3}	—	—	—	—	—	—	—	—

Notations (h_1), (h_2), (h_3) denote that the corresponding results are obtained on three successive meshes with mesh size $h_1 = 8.84\times10^{-2}$, $h_2 = 4.42\times10^{-2}$ and $h_3 = 2.21\times10^{-2}$, respectively.

Copyright © 2010 John Wiley & Sons, Ltd.

DOI: 10.1002/fld

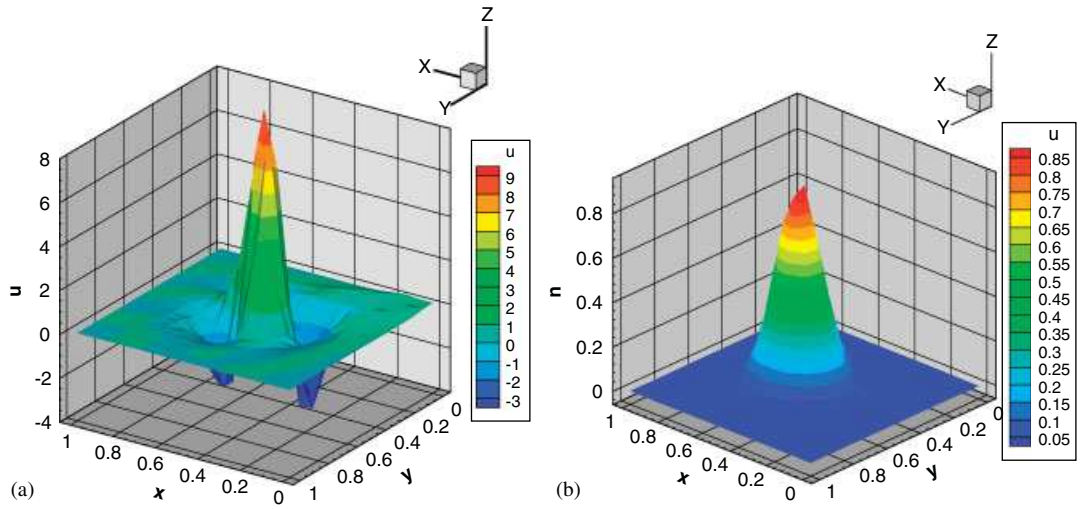

Figure 16. Test 4: The MFEM and LPEW2 solution for $\alpha = 1000$ on the coarse mesh: (a) MFEM and (b) LPEW2.

respectively, on the coarse mesh, and on the finer mesh these oscillations are reduced (`umin` $= -2.71 \times 10^{-3}$, `umax` $= 0.992$).

- The solution errors with LPEW2 are much smaller than with MFEM for various anisotropy.
- The convergence rates for the edge normal flux errors with MFEM and LPEW2 are very close, and LPEW2 shows a little better than MFEM.

Finally, it should be noted that the scheme LPEW2 performs best among all the four schemes in this test and meshes, and is robust and efficient in the range of anisotropy ratio 1–1000.

3.5. *Test 5*: *numerical locking*

In this test, we consider the problem (1a) on a unit square domain $\Omega = [0, 1]^2$ with the diffusion tensor

$$K = \begin{pmatrix} 1 & 0 \\ 0 & \delta \end{pmatrix},$$

and the exact solution $u(x, y) = \sin(2\pi x)\mathrm{e}^{-2\pi y\sqrt{1/\delta}}$ which is dependent on δ in the y-direction so that the force term equals to zero. Note that the minimum and maximum values of the solution are located on the boundary, and thus are difficult to obtain with the Neumann boundary conditions. Since δ is large, the solution is almost constant in the y variable.

In Test 5, we consider the following settings for the definitions of boundaries Γ_D and Γ_N:

- Case A: fully Dirichlet boundary condition ($\Gamma_N = \emptyset$);
- Case B: mixed boundary condition

$$\Gamma_D = \{(x, y) | x = 0 \text{ or } y = 0\}, \quad \Gamma_N = \partial\Omega \backslash \Gamma_D;$$

- Case C: nearly pure Neumann boundary condition

$$\Gamma_D = \{(x, y) | 1 - h \leqslant x \leqslant 1 \text{ and } 1 - h \leqslant y \leqslant 1\}, \quad \Gamma_N = \partial\Omega \backslash \Gamma_D.$$

Case C can be treated as a modification of the fully Neumann boundary condition. The Dirichlet boundary condition is imposed on two boundary edges at the top-right corner and the length of them tends to zero as the mesh size $h \to 0$.

To our knowledge, a locking effect [13, 28] may arise for strong anisotropy when solving the anisotropic diffusion model and can be experimentally observed when the discretization error does

Copyright © 2010 John Wiley & Sons, Ltd.

DOI: 10.1002/fld

Table V. Test 5: minimum and maximum solutions for LPEW1 on the triangular mesh (Mesh1) with mesh size $h=0.125$ for various anisotropy ratios.

	$\delta=1$		$\delta=10^2$		$\delta=10^4$		$\delta=10^6$	
Problem	umin	umax	umin	umax	umin	umax	umin	umax
Case A	−0.716	0.716	−0.899	0.899	−0.935	0.935	−0.948	0.948
Case B	−0.714	0.717	−0.898	0.898	−0.944	0.947	−0.987	0.994
Case C	−0.838	0.838	−0.977	1.140	−0.890	0.777	−0.890	0.792

Table VI. Test 5: minimum and maximum solutions for LPEW2 on the triangular mesh (Mesh1) with mesh size $h=0.125$ for various anisotropy ratios.

	$\delta=1$		$\delta=10^2$		$\delta=10^4$		$\delta=10^6$	
Problem	umin	umax	umin	umax	umin	umax	umin	umax
Case A	−0.716	0.716	−0.897	0.897	−0.931	0.931	−0.935	0.935
Case B	−0.714	0.717	−0.895	0.895	−0.929	0.930	−0.933	0.934
Case C	−0.838	0.838	−0.858	0.993	−0.773	0.992	−0.769	0.995

not decrease at the expected rate for the limiting anisotropic values. Test 5 was introduced in [13, 29] with a slight modification as causing some numerical locking problems for the schemes and was also used as a benchmark in the FVCA5 conference [25]. In fact some schemes could not give the solution. Severe locking effects have been reported especially in Case C [28–30].

The meshes we consider here are the strictly acute triangular meshes (Mesh1), and the performance of LPEW1 and LPEW2 will be investigated by calculating the solution errors and edge normal flux errors on a sequence of successively refined triangular meshes for increasing anisotropy in Case A–Case C.

In Tables V and VI, we present the minimum and maximum values of the solution for various anisotropy δ on the coarse mesh with mesh size $h=0.125$. Since the exact solution is located in the interval $[-1, 1]$, almost all values satisfy the discrete maximum principle for LPEW1 and LPEW2 except that the scheme LPEW1 exceeds the maximum value 1 on Case C for $\delta=10^2$.

All the convergence behaviors for LPEW1 and LPEW2 are plotted in Figures 17 and 18 as log–log plots of the L^2 norms of the solution errors and edge normal flux errors versus the characteristic mesh size h, and we maintain the consistency of the plot scales so that all figures can be easily comparable. The results for the scheme LPEW1 in Figure 17 show the following:

- The scheme LPEW1 has a second-order convergence rate with respect to the solution errors for Case A–Case C with $\delta\leqslant 10^2$.
- The convergence of edge normal flux for LPEW1 is of the order $h^{1.5\sim 2}$ in Case A–Case C with anisotropy $\delta\leqslant 10^2$.
- For anisotropy $\delta\geqslant 10^3$, the convergence of LPEW1 is broken on the fine meshes and a strong locking effect is visible.

Compared with Figure 17, the results for the scheme LPEW2 in Figure 18 reveal the following facts:

- The scheme LPEW2 has a second-order convergence rate with respect to the solution errors and edge normal flux errors for Case A and Case B, and for increasing anisotropy δ, the convergence curves for the solution is almost the same and the solution error is deteriorated by a factor of about 1.3 going from the isotropic to the most anisotropic case.
- In Case C, the presence of nearly pure Neumann boundary conditions enhances the difficulties introduced by the strong anisotropy. A locking effect is visible in Case C, and there are two symptoms: the solution error constant increases as the anisotropy δ increases; for δ up to 10^3, there involve unfeasible calculations on the fine meshes with mesh size $h\leqslant 3.12\times 10^{-2}$.
- The scheme LPEW2 performs better than LPEW1 in this test for the triangular meshes (Mesh1).

Copyright © 2010 John Wiley & Sons, Ltd.

DOI: 10.1002/fld

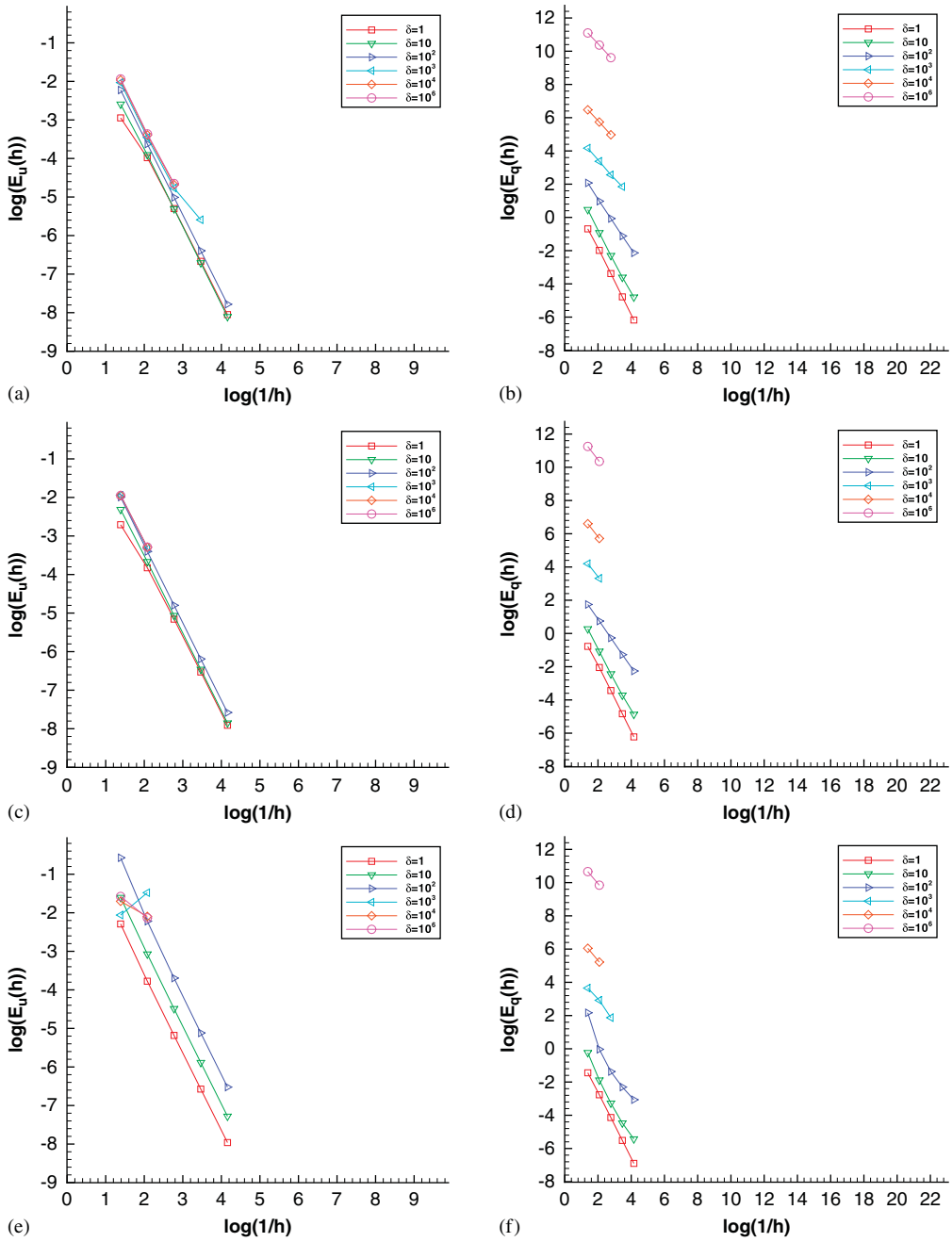

Figure 17. Test 5: L^2 error curves for the scheme LPEW1 on the triangular mesh (Mesh1): (a) Case A: solution; (b) Case A: edge normal flux; (c) Case B: solution; (d) Case B: edge normal flux; (e) Case C: solution; and (f) Case C: edge normal flux.

Finally in this test, the scheme LPEW2 can overcome or strongly reduce the numerical locking phenomenon in many cases for the triangular meshes (Mesh1).

4. CONCLUSION

In this paper we suggest the linearity-preserving cell-centered scheme, which is robust and reliable in the solution of strongly anisotropic heterogeneous diffusion problems on general distorted

Copyright © 2010 John Wiley & Sons, Ltd.

DOI: 10.1002/fld

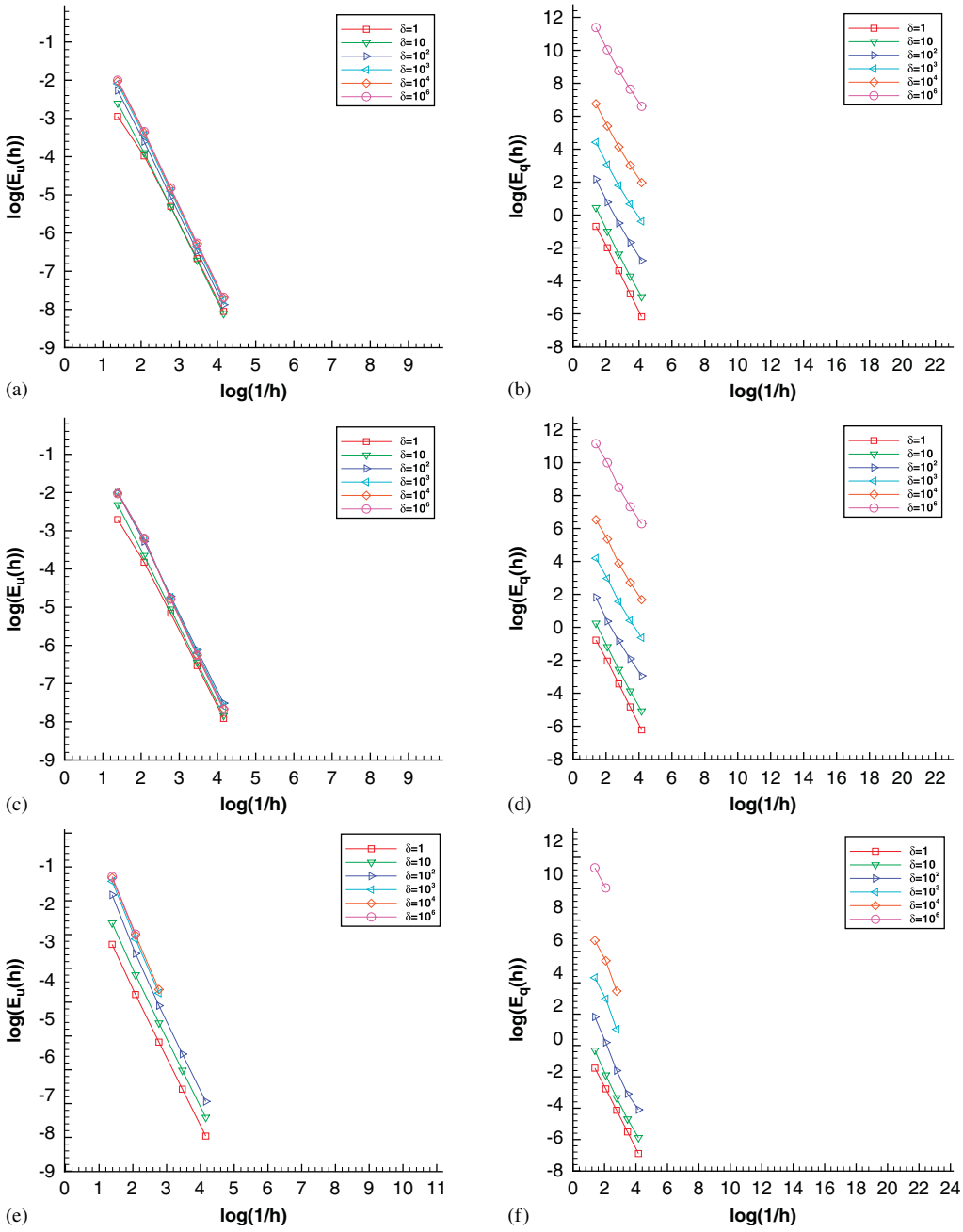

Figure 18. Test 5: L^2 error curves for the scheme LPEW2 on the triangular mesh (Mesh1): (a) Case A: solution; (b) Case A: edge normal flux; (c) Case B: solution; (d) Case B: edge normal flux; (e) Case C: solution; and (f) Case C: edge normal flux.

(possibly nonconforming) meshes. The scheme allows arbitrary diffusion tensors, and the computation of the weights in the scheme is neither discontinuity dependent nor mesh topology dependent. Many dedicate experiments using meshes with unstructured, severely distorted and nonmatching elements and arbitrary (continuous or discontinuous, homogeneous or heterogeneous) anisotropic diffusion tensors show the good performance of the proposed scheme (quadratic convergence rate for the approximate solution and higher than first-order accuracy for the discrete flux).

Copyright © 2010 John Wiley & Sons, Ltd.

DOI: 10.1002/fld

ACKNOWLEDGEMENTS

The authors thank the anonymous reviewers for their carefully readings and many useful suggestions.

This work is supported by the National Natural Science Fundation of China (Nos. 11001025,10871030, 10635050, 11071024) and a grant from the Laboratory of Computational Physics.

REFERENCES

1. Morel J, Dendy J, Hall M, White S. A cell-centered Lagrangian-mesh diffusion differencing scheme. *Journal of Computational Physics* 1992; **103**:286–299.
2. Shashkov M, Steinberg S. Solving diffusion equations with rough coefficients in rough grids. *Journal of Computational Physics* 1996; **129**:383–405.
3. Morel JE, Roberts RM, Shashkov MJ. A local support-operators diffusion discretization scheme for quadrilateral $r-z$ meshes. *Journal of Computational Physics* 1998; **144**:17–51.
4. Breil J, Maire PH. A cell-centered diffusion scheme on two-dimensional unstructured meshes. *Journal of Computational Physics* 2007; **24**:785–823.
5. Chang LN, Yuan GW. Cell-centered finite volume methods with flexible stencils for diffusion equations on general nonconforming meshes. *Computer Methods in Applied Mechanics and Engineering* 2009; **198**:1638–1646.
6. Huang WZ, Kappen AM. A study of cell-center finite volume methods for diffusion equations. *Mathematics Research Report 98-10-01*, Department of Mathematics, University of Kansas, Lawrence, KS, 1998.
7. Wu JM, Fu SW, Shen LJ. A difference scheme with high resolution for the numerical solution of a nonlinear diffusion equation (in Chinese). *Journal on Numerical Methods and Computer Applications* 2003; **24**:116–128.
8. Wu JM. Linearly exact method and the difference scheme for diffusion equation on quadrilateral meshes. *Annual Report*, Laboratory of Computational Physics, Institute of Applied Physics and Computational Mathematics, Beijing, China, 2005; 156–169.
9. Basko MM, Maruhn J, Tauschwitz A. An efficient cell-centered diffusion scheme for quadrilateral grids. *Journal of Computational Physics* 2009; **228**:2175–2193.
10. Lv GX, Shen LJ, Shen ZJ. Numerical methods for energy flux of diffusion equation on unstructured grids (in Chinese). *Chinese Journal of Computational Physics* 2007; **24**(4):379–386.
11. Zhao Q, Yuan GW. Analysis and construction of cell-centered finite volume scheme for diffusion equations on distorted meshes. *Computer Methods in Applied Mechanics and Engineering* 2009; **198**(37–40):3039–3050.
12. Coudière Y, Vila J-P, Villedieu P. Convergence rate of a finite volume scheme for a two-dimensional diffusion convection problem. *Mathematical Modelling and Numerical Analysis* 1999; **33**(3):493–516.
13. Manzini G, Putti M. Mesh locking effects in the finite volume solution of 2-d anisotropic diffusion equations. *Journal of Computational Physics* 2007; **220**(2):751–771.
14. Sheng ZQ, Yuan GW. A nine point scheme for the approximation of diffusion operators on distorted quadrilateral meshes. *SIAM Journal on Scientific Computing* 2008; **30**:1341–1361.
15. Wu JM, Dai ZH, Gao ZM, Yuan GW. Linearity preserving nine-point schemes for diffusion equation on distorted quadrilateral meshes. *Journal of Computational Physics* 2010; **229**(9):3382–3401.
16. Lipnikov K, Shashkov M, Yotov I. Local flux mimetic finite difference methods. *Numerische Mathematik* 2009; **112**:115–152.
17. Aavatsmark I, Barkve T, Bøe Ø, Mannseth T. Discretization on non-orthogonal, quadrilateral grids for inhomogeneous, anisotropic media. *Journal of Computational Physics* 1996; **127**:2–14.
18. Klausen RA, Winther R. Robust convergence of multipoint flux approximation on rough grids. *Numerische Mathematik* 2006; **104**:317–337.
19. Chen QY, Wan J, Yang Y, Mifflin RT. Enriched multi-point flux approximation for general grids. *Journal of Computational Physics* 2008; **227**:1701–1721.
20. Wheeler MF, Yotov I. A multipoint flux mixed finite element method. *SIAM Journal on Numerical Analysis* 2006; **44**:2082–2106.
21. Aavatsmark I, Eigestad GT, Klausen RA, Wheeler MF, Yotov I. Convergence of a symmetric mpfa method on quadrilateral grids. *Computational Geosciences* 2007; **11**:333–345.
22. Li DY, Shui HS, Tang MJ. On the finite difference scheme of two-dimensional parabolic equation in a non-rectangular mesh (in Chinese). *Journal on Numerical Methods and Computer Applications* 1980; **1**:217–224.
23. Hermeline F. Approximation of diffusion operators with discontinuous tensor coefficients on distorted meshes. *Computer Methods in Applied Mechanics and Engineering* 2003; **192**:1939–1959.
24. Aavatsmark I, Eigestad GT, Mallison BT, Nordbotten JM. A compact multipoint flux approximation method with improved robustness. *Numerical Methods for Partial Differential Equations* 2008; **24**:1329–1360.
25. Herbin R, Hubert F. Benchmark on discretization schemes for anisotropic diffusion problems on general grids. In *Finite Volumes for Complex Applications V—Problems and Perspectives*, Eymard R, Herard J-M (eds). Wiley: New York, 2008; 659–692.
26. Younes A, Fontaine V. Efficiency of mixed hybrid finite element and multipoint flux approximation methods on quadrangular grids and highly anisotropic media. *International Journal for Numerical Methods in Engineering* 2008; **76**:314–336.

Copyright © 2010 John Wiley & Sons, Ltd.

DOI: 10.1002/fld

27. Breil J, Maire P-H, Nicolai P, Schurtz G. Modelling of the magnetic field effects in hydrodynamic codes using a second order tensorial diffusion scheme. *Journal of Physics*: *Conference Series* 2008; **112**:1–4.
28. Havu V. An analysis of asymptotic consistency error in a parameter dependent model problem. *Calcolo* 2003; **40**(2):121–130.
29. Babuska I, Suri M. On locking and robustness in the finite element method. *SIAM Journal on Numerical Analysis* 1992; **29**(5):1261–1293.
30. Havu V, Pitkaranta J. An analysis of finite element locking in a parameter dependent model problem. *Numerische Mathematik* 2001; **89**(4):691–714.

Copyright © 2010 John Wiley & Sons, Ltd.

DOI: 10.1002/fld